

5-2017

## Characterization of Coupled Gold Nanoparticles in a Sparsely Populated Square Lattice

Roy Truett French III  
*University of Arkansas, Fayetteville*

Follow this and additional works at: <https://scholarworks.uark.edu/etd>



Part of the [Nanoscience and Nanotechnology Commons](#), [Nanotechnology Fabrication Commons](#), and the [Optics Commons](#)

---

### Citation

French, R. T. (2017). Characterization of Coupled Gold Nanoparticles in a Sparsely Populated Square Lattice. *Graduate Theses and Dissertations* Retrieved from <https://scholarworks.uark.edu/etd/1927>

This Thesis is brought to you for free and open access by ScholarWorks@UARK. It has been accepted for inclusion in Graduate Theses and Dissertations by an authorized administrator of ScholarWorks@UARK. For more information, please contact [uarepos@uark.edu](mailto:uarepos@uark.edu).

Characterization of Coupled Gold Nanoparticles in a Sparsely Populated Square Lattice

A thesis submitted in partial fulfillment  
of the requirements for the degree of  
Master of Science in MicroElectronics-Photonics

by

Roy Truett French III  
University of Central Arkansas  
Bachelor of Science in Physics and Mathematics, 2011  
University of Arkansas  
Master of Science in Physics, 2014

May 2017  
University of Arkansas

This thesis is approved for recommendation to the Graduate Council.

---

Dr. D. Keith Roper  
Thesis Director

---

Dr. R. Panneer Selvam  
Committee Member

---

Dr. Morgan Ware  
Committee Member

---

Dr. Rick Wise  
Ex-Officio Member

## **ABSTRACT**

Metal nanoparticles deposited in regular arrays spaced at optical wavelengths support a resonance due to a coherent coupling between localized surface plasmon mode and lattice diffraction allowing for engineering of tunable devices for use in biological sensors, nanoantennae, and enhanced spectroscopy. Techniques such as electron beam lithography, focused ion beam lithography, nanosphere lithography, and nanoimprint lithography are used for fabrication but are limited by cost, device throughput, and small deposition. Polymer soft lithography and continuous dewetting of particles is a potentially viable alternative showing promise in all of those areas. This thesis developed the fabrication of a refined hydrophilic nanoimprinted polymer substrate with a regular square lattice and characterized the optical response of sparsely deposited nanoparticles by continuous dewetting which permit a diffractive lattice coupling.

The following signatories attest that all software used in this thesis was legally licensed for use by Mr. Roy T. French III for research purposes and publication.

---

Mr. Roy T. French III  
Student

---

Dr. D. Keith Roper  
Thesis Director

This thesis was submitted to <http://www.turnitin.com> for plagiarism review by the TurnItIn company's software. The signatories have examined the report on this thesis that was returned by TurnItIn and attest that, in their opinion, the items highlighted by the software are incidental to common usage and are not plagiarized material.

---

Dr. Rick Wise  
Program Director

---

Dr. D. Keith Roper  
Thesis Director

## ACKNOWLEDGMENTS

I would like to acknowledge and thank my advisor, Dr. Keith Roper, whose mentorship has been pivotal in my growth as a graduate student. It has been an honor these last three years working with him learning about the field of plasmonics, developing new ideas, and making new discoveries that could shape the future. I always leave every group meeting inspired, and excited about the next scientific adventure, and for that, I am thankful.

To all the members of the NanoBio photonics group, past and present, I want to thank you for all of your guidance and help along my journey as a graduate student. In particular, I would like to thank Vinith Bejugam without whom this project would not have seen the same conclusions. Vinith has been a great collaborator who was with me every day, spending hours developing the fabrication technique, performing experiments, and gazing in a microscope characterizing sample after sample. To you, Vinith, I am so very thankful having shared this experience and being able to walk away with a good friend and work colleague. I would also like to thank Gregory T. Forcherio for taking the time to explain all of the equipment needed for this experiment and all of the countless hours spent discussing ideas surrounding this experiment as well as guiding me in my studies. I am grateful to Manoj Seeram for helping develop the MATLAB code used in the experiment and Dr. Phillip Blake and James Proctor for further development of the negative imprinting technique used. Thank you, Drew DeJarnette and Gregory T. Forcherio, for providing theoretical simulations.

The training and guidance I received from faculty and mentors at the University of Central Arkansas Physics department was crucial in my development as a scientist. I would like to thank Dr. William V. Slaton for his mentorship through my four years in the physics program.

He had faith in my lab skills and helped me develop them further. I would like to thank Dr. Stephen Addison for encouraging me to pursue a graduate degree.

I would like to thank my parents, Roy and Karen, whose love and support has made me who I am. Thank you so very much for inspiring me every day of my life, encouraging me to think critically, and supporting me in the pursuits of my dreams.

Lastly, I would like to thank my wife, Amber, who has been a beacon of hope and encouragement. She has supported me throughout my entire graduate career offering personal advice, guidance, and most importantly, love and laughter. My accomplishments are your accomplishments.

## TABLE OF CONTENTS

Chapter 1 – Emergent Systems .....	1
1.1 What is Emergent Behavior? .....	1
1.2 Examples of Emergent Systems.....	4
1.3 Additive Versus Emergent Plasmonic Systems .....	5
1.4 Research Objective .....	6
Chapter 2 – Plasmonic Metamaterials .....	9
2.1 Plasmon Resonance .....	9
2.2 Coupled Resonances in Nanoparticle Lattices.....	10
2.3 Disordered Nanoparticle Lattices .....	11
2.4 Fano Resonance .....	12
2.4.1 Classical Analogy to Fano Resonance.....	13
2.4.2 Parameter Free Model for Fano Resonance in Plasmonic Structures .....	16
2.5 Mie Theory.....	19
2.6 Summary .....	22
Chapter 3 - Fabrication and Characterization of Two-Dimensional Arrays.....	24
3.1 Fabrication Methods .....	24
3.2 Soft lithography and Poly(dimethylsiloxane-b-ethylene oxide).....	26
3.2 Materials and Equipment .....	27
3.3 Stamp Fabrication and Particle Deposition.....	27
3.4 Procedure for Capturing Images and Spectra .....	30
3.5 Summary .....	31
Chapter 4 - Characterization of Sparsely Deposited Gold Nanoparticle Arrays .....	33
4.1 Analysis of Sparse Array Using Diascopic Illumination .....	33
4.2 Analysis of Sparse Array Using Episcopic Illumination .....	36
4.3 <i>In silico</i> Analysis of Optically Active Nodes by Use of Photometric Properties of AuNPs .....	38
4.4 Particle Chain Size Distribution and Emergence of Fano Resonance .....	41
4.5 One-Dimensional and Two-Dimensional Array Comparisons of Coupled Dipole Models with Experimental Results .....	44
4.6 Summary .....	45
Chapter 5 - Concluding Remarks.....	47
5.1 Importance of Work .....	47
5.2 Research Summary .....	48

5.3 Future Work .....	50
References .....	52
APPENDIX.....	59
A: Description of Research for Popular Publication.....	59
B: Executive Summary of Newly Created Intellectual Property .....	61
C: Possible Patent and Commercialization Aspects of Intellectual Property .....	62
D: Broader Impact of Research.....	64
E: Microsoft Project for Master’s Microelectronics-Photonics Degree Plan .....	66
F: Identification of All Software Used in Thesis Generation .....	67
G: All Publications Published, Submitted, and Planned.....	68

## LIST OF FIGURES

Figure 1.1. Example of two sets of arrays representing two possible scenarios for sparsity.....	7
Figure 1.2. Fano resonant plasmonic analogue for a two-dimensional array.....	8
Figure 2.1. Dipolar plasmon of a gold nanosphere created by incident light.....	10
Figure 2.2. Schematic of two weakly coupled particles.....	14
Figure 2.3. Mechanism for broadband plasmonic coupling by incident light.....	17
Figure 2.4. Single particle Mie theory comparison with experimental data.....	22
Figure 3.1. Fabrication of nanopatterned PDMS-PEO stamp for particle deposition.....	28
Figure 3.2. Square grid of cavities.....	29
Figure 3.3. Continuous dewetting process of gold nanoparticles into PDMS-PEO stamp.....	30
Figure 3.4. Comparison of smoothed and unsmoothed spectra for episcopic illumination.....	31
Figure 4.1. Illustration of the setup used for diascopic characterization of the sample.....	34
Figure 4.2. Diascopic characterization of AP and CLR features for varying areas of sparsity....	35
Figure 4.3. Illustration of the setup used for episcopic characterization of the sample.....	37
Figure 4.4. Episcopic characterization of AP and CLR features for varying areas of sparsity....	38
Figure 4.5. Illustration for counting particles manually, and computationally using luma.....	41
Figure 4.6. Chain size distributions for areas captured in episcopic mode.....	42
Figure 4.7. Magnitudes of intensity versus median chain size from episcopic characterization..	42
Figure 4.8. Logarithmic and non-linear intensity magnitude versus number of particles.....	45

## LIST OF TABLES

Table 3.1. Summary of common methods to obtain arrays of nanostructures.....	25
--	----

## Chapter 1 – Emergent Systems

In the physical sciences, students begin training to understand how a macroscopic entity interacts with other macroscopic entities. On this scale, Newtonian Laws describe macroscopic behaviors. For even larger scales, i.e., astronomical units, the theory of relativity can be used to determine how stars will behave in a binary system, or how exactly light bends around massive objects. Later in a student's career in the physical sciences they begin to study the opposite end of the spectrum: microscopic entities. The peculiar world of quantum mechanics will begin to shed light on why an atom will have particular properties, as well as give insight into how particles behave together. Quantum mechanics can even give insight into single particle entities. In learning these concepts, one will begin to recognize that individual particles can combine together and the system that is made will behave vastly different than if the particles were by themselves. This collective, emergent behavior has fascinated scientists for decades and rightfully so because there is one fundamental reality stemming from it: life. In this chapter, the author will define and discuss emergent phenomena and give several examples of where the concepts help to understand certain phenomena in the world. A brief discussion on the relation to the experiment performed in this thesis will also be given.

### 1.1 What is Emergent Behavior?

Emergence, or emergent behavior, is the idea that a collection of singular entities coherently combine and work together to provide an outcome that cannot otherwise be obtained by the singular entity.<sup>1</sup> An example of this is the atom. Atoms are a collection of elementary particles like the electron and those that make up the proton and neutron. These atoms can further be combined to make molecules, and those molecules can be combined to create cells that

eventually can lead to creating life. One particularly interesting example of this is a molecular motor such as a motor protein. Motor proteins are molecules that are combined and together they carry proteins in the cytoplasm through chemical reactions. Aristotle was probably the first to define this type of behavior: “things which have several parts and in which the totality is not, as it were, a mere heap, but the whole is something beside the parts.”<sup>2</sup> The more common phrase is the whole is greater than the sum of its parts.

This idea of emergence and its relation to life was birthed from a book Erwin Schrödinger wrote in 1944 titled “What is Life?” wherein he tried to connect thermodynamics with life.<sup>3</sup> The book is based on a collection of lectures he gave where he began by asking the question how can physics and chemistry explain the processes that occur in living organisms? He importantly noted that even though the sciences of his time could not explain those processes it was not to say that they could not; in fact, in current times, biophysics and biochemistry have made substantial progress in explaining how bioprocesses work and solving questions that could have potential applications in curing certain diseases.<sup>4</sup>

The crux of his book is the idea of “order from disorder” and “order from order”. In a way, these terms define emergence because complex systems can be created from singular disordered entities that come together to form an ordered arrangement. Entropy is a particularly important notion in emergent systems and is also a very fundamental part of thermodynamics. The second law of thermodynamics states that the total entropy in an isolated closed system always increases over time. Schrödinger used this idea of entropy to discuss life as an emergent system providing examples such as Brownian motion, diffusion, and gene mutation to help the discussion. Schneider et al. used his ideas about order from disorder to better connect microbiology with physics.<sup>1</sup>

In general, there are three different types of systems whose behaviors are explored by thermodynamics. The first system exhibits classical behavior where molecules in a closed system at equilibrium interact with each other. The second system is slightly perturbed from equilibrium but will return back to equilibrium. An example of this is having a partitioned box of two sides, call them A and B, that are connected via a wall that has a door. Suppose that there are more particles in partition A than B, when the door is opened between the two partitions the particles will eventually move so that partition A and B have reached an equilibrium with the same number of molecules on average. The last type of systems contains gradients that constrain the system to remain away from equilibrium, referred to as a non-equilibrium quasi-stable state. An example of this is the same as that described for the second type of system but with an added pressure gradient so that partition A contains more particles than partition B. These systems, unlike the others, allow the flow of energy or material into and out of the system and are defined as dissipative systems. Dissipative systems tend to be emergent, for example non-living organized entities such as tornadoes and living organisms. Their total entropy is the addition of internal entropy and the entropy exchanged with their environment. If an ordered organization persists in a non-equilibrium steady state, the entropy should be negative. Certainly, one may think that this would violate the second law of thermodynamics, but the idea that entropy must increase applies to closed systems that are adiabatically isolated. Since a dissipated system is an open system which allows heat and/or material to leave and enter, there is no violation of this law; the system will export more entropy to maintain its low entropy and keep the total entropy high.

Schneider et al. put forth a corollary to the Unified Principle of Thermodynamics stated by Joseph Kestin<sup>5</sup> to help understand these types of dissipative, emergent systems: “As systems

are moved away from equilibrium, they will utilize all avenues available to counter the applied gradients. As the applied gradients increase, so does the system's ability to oppose further movement from the equilibrium." Thermodynamics systems tend to resist gradients that will move them from their equilibrium position and Schneider et al. note that more sophisticated structures and mechanisms are created as these gradients become stronger and stronger, ultimately leading to self-organization processes to counteract these gradients. These complex "emergent systems" are referred to as gradient dissipaters.

## **1.2 Examples of Emergent Systems**

In the previous section a brief description was provided to give background on emergent systems, particularly dissipative systems. The idea of emergent systems has been generalized, though, over the decades to simply mean any system that provides a response that is only achievable through coherent cooperation of singular entities. This idea can be applied to biology, nature, technology, etc. For example, NASA has been studying how to use the idea of emergence to create robotic spacecraft that would study the asteroid belt with their Autonomous Nano Technology Swarm (ANTS) mission.<sup>6</sup> This mission includes 1,000 individual robotic spacecraft that would work together to study the asteroid belt. Emergent behavior is key for this caliber of a mission because the spacecraft could be out of range of contact with NASA and, thus, the unit as a whole needs to be able to collaboratively work together to achieve the desired results. These robotic spacecraft would operate on low-bandwidth signals due to weight constraints making it difficult for NASA to see the operational behavior of the swarm and correct any errors. The swarm, therefore, must work together as a whole unit in order to study the asteroid belt.

NASA is not the only group interested in projects aimed at research into emergent

systems. The Computer Science Department at University of York has created the Theory Underpinning Nanotech Assembly project, TUNA for short.<sup>7</sup> This project aims to investigate emergent engineering for use in molecular nanotechnology by studying the feasibility of engineering techniques to model, analyze, and simulate nanoscale systems. The group is using haemostasis, i.e. staunching of bleeding, as the case study and developing software techniques and computer simulations to theoretically assemble nanites that would achieve that goal. Use of these case studies and the development of programs to create emergent behaviors under different environmental factors will hopefully one day help scientists better engineer emergent systems.<sup>7</sup>

Another example of emergent behavior can be found with geometrically frustrated magnets, with specific focus on  $\text{ZnCr}_2\text{O}_4$ . Magnetism in a transition metal oxide occurs because of the atomic spin alignment at the vertices of its periodic lattice. Periodic lattices that have corner sharing tetrahedra, as is the case in  $\text{ZnCr}_2\text{O}_4$ , contain a complex alignment of spins that leads to geometrical frustration; geometrical frustration occurs in condensed matter when there are inter-atomic forces in the crystal lattice that are conflicting. By studying quasi-elastic scattering of neutrons with  $\text{ZnCr}_2\text{O}_4$ , Lee et al. were the first to demonstrate an emergent confined spin cluster degree of freedom.<sup>8</sup>

### **1.3 Additive Versus Emergent Plasmonic Systems**

Not all systems that include an ensemble of singular entities are emergent. In contrast to emergent systems, additive systems are systems whose constituents combine linearly together to provide an overall enhancement of an advantageous property provided by a singular entity.<sup>9</sup> For example, a nanomesh of nanorods can provide an enhancement in plasmonic absorbance. But what would happen if the nanorods are placed in an ordered array? The array would facilitate the

emergence of properties that would otherwise not occur without the array.<sup>10,11</sup> In recent years there has been a lot of interest in using arrays of plasmonic nanoparticles due to their ability to coherently couple.<sup>12, 13, 14</sup> Known as Coupled Lattice Resonance (CLR), particles in an array architecture are able to coherently couple due to in-plane diffractive scattering. The resulting spectra for arrays of plasmonic nanoparticles show a Fano resonant signature. Couple Lattice Resonance and Fano resonance will be further elaborated in Chapter 2 of this thesis along with a brief introduction to plasmonics but are introduced here to identify them as emergent phenomena that arise due to an array of nanoparticles. These resonances are not additive because two spectral signatures can be measured: one from the plasmonic activity of the particles in the array defined here as the lattice plasmon resonance (LPR), and a second from the resonant coupling of diffracted light that relies on the lattice pitch of the array.

#### **1.4 Research Objective**

This thesis will focus on the creation of a sparse array in which coherent coupling dynamically emerges as the population of nanoparticles increases. Sparsity in this context is defined as a lack of nodal elements in the array that results in ensembles of vertical chains of particles with varying lengths. In this thesis, these particles will be referred to as optically active nodes because of their optical plasmonic activity and their placement in a lattice configuration. Take, for example, the leftmost array in Figure 1.1 as a possible sparse array of optically active nodes. Random additions of optically active nodes decrease the sparsity, and creates chains of optically active nodes with varying lengths (see the rightmost array in Figure 1.1). When horizontally polarized light is incident on the optically active nodes, the optically active nodes in columns in the array are able to couple with diffracted light rays because of how the dipolar

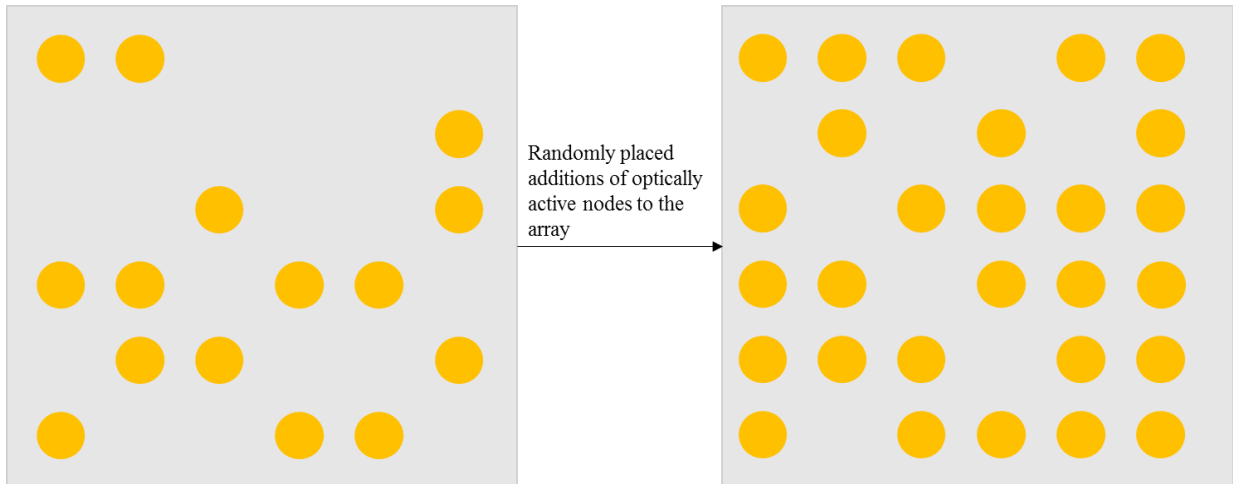


Figure 1.1. Example of two sets of arrays representing two possible scenarios for sparsity. Additions of randomly placed particles in the array decreases sparsity, as seen in the right array. Addition of these nodal elements causes increases in vertical chain lengths of the nodal elements.

localized surface plasmon resonance (LSPR) is created (see Figure 1.2 for a schematic representation). The coupling of the particle plasmon with diffracted light gives rise to an emergent Fano resonant CLR. Vertically polarized light could also be used, but instead of columns of optically active nodes coupling with diffracted light from the array, optically active nodes in the rows would couple.

The emergence of far-field diffraction signatures was obtained using an all-optical approach that quantified population density of nanoparticles and their order distribution. An all-optical approach was required because the selected medium to fabricate the array was the polymer polydimethylsiloxane (PDMS)-polyethylene oxide (PEO). Scanning electron (SEM) images are traditionally used to observe nanoparticles, however, SEM is refractive to polymers causing charging effects which distort the image, necessitating the need for an all-optical description. Furthermore, the minimum number of nanoparticles required that could provide signatures of emergent coherent diffractive coupling was also explored by statistical and image analysis of gold (Au) nanoparticles (NPs) self-assembled into square cavities imprinted into a

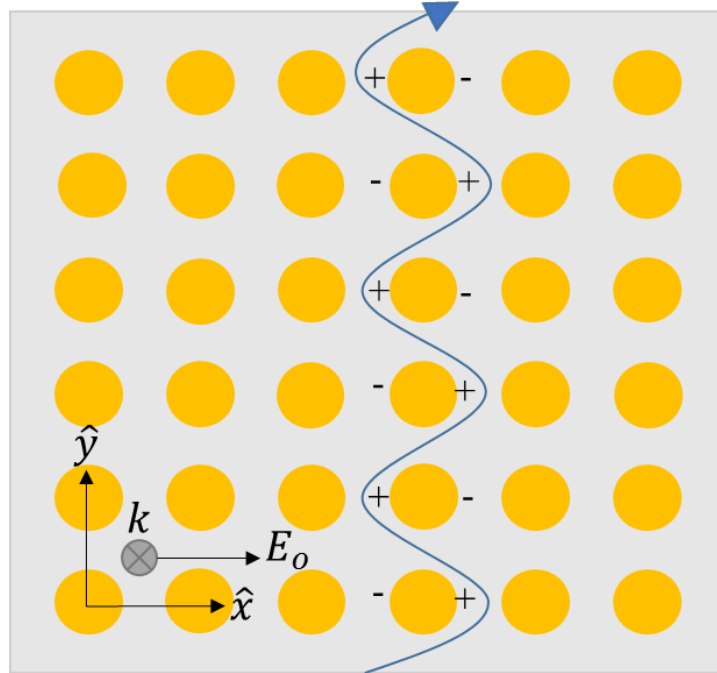


Figure 1.2. Fano resonant plasmonic analogue for a two-dimensional array. Horizontally polarized incident light excites the plasmon resonance of the optically active nodes. Diffracted light rays couple with the optically active nodes creating a CLR.

PDMS-PEO substrate. Remarkably, coherent coupling can still be obtained for these types of sparse systems because emergent systems have an inherent resilience to single-point failures.<sup>10</sup>

## Chapter 2 – Plasmonic Metamaterials

Plasmonic metamaterials are artificially engineered materials that are not found in nature, where incorporation of noble metal plasmonic nanoparticles allows for manipulation of electromagnetic energy at the nanoscale. Periodic ordering of nanoparticles produces diffractive modes which change the plasmonic resonance and introduces a secondary coupled lattice resonance (CLR). This chapter provides a background on plasmonic nanoparticles, coupled systems of plasmonic nanoparticles, and provides a review of current literature on disordered systems.

### 2.1 Plasmon Resonance

Nanoscale noble metals are able to manipulate electromagnetic energy through the production of plasmons.<sup>15</sup> Plasmons are a coherent oscillation of the free electron gas in metals that are confined to the metal-dielectric interface.<sup>16,17</sup> Metal nanoparticles support plasmons that are confined to the surface of the particle and are referred to as localized surface plasmon resonance (LSPR) and are dependent on the size of the particle,<sup>18,19</sup> shape,<sup>16,18,20,21</sup> and composition. Plasmonic devices have applications in Raman spectroscopy,<sup>22</sup> heating,<sup>23,24,25</sup> photovoltaics, and enhancement of charge carriers in semiconductor devices<sup>15,26</sup> because of the intense near-fields that are created. Refractive index sensing is another application for plasmonic devices because plasmons are dependent on the local environmental refractive index where shifts in the absorbance spectra occur with changing refractive index.<sup>27,28,29</sup> Figure 2.1 shows an example of an LSPR for two gold spheres. Incident light with frequency equal to the nanoparticles plasma frequency causes an oscillatory motion of the conduction electrons in the metal.

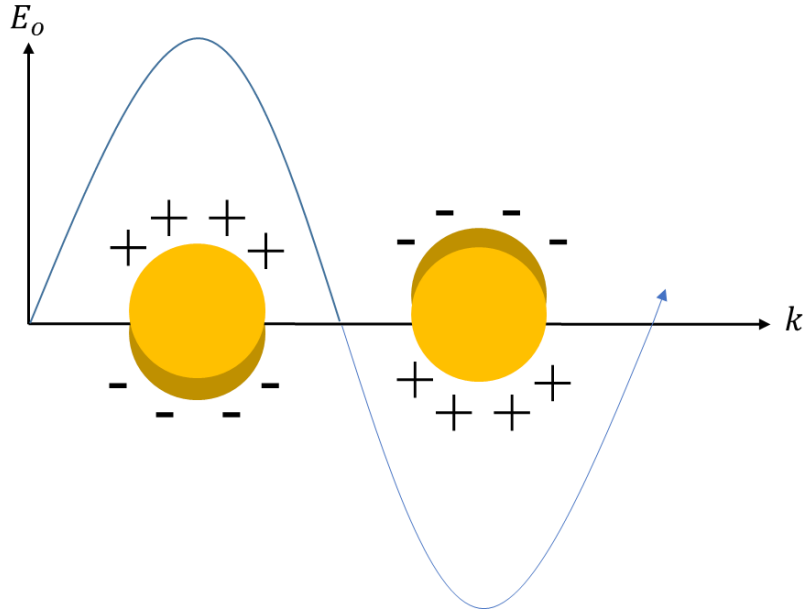


Figure 2.1. Dipolar plasmon of a gold nanosphere created by incident light where  $E_0$  is the amplitude of the electric field and  $k$  is the wave vector.

## 2.2 Coupled Resonances in Nanoparticle Lattices

Nanostructures configured into periodic lattices whose spacing is above the LSPR wavelength can support Fano-resonant coupling between far-field diffractive modes and near-field plasmon modes.<sup>30–33</sup> Plasmonic nanoparticles in arrays are weakly coupled to diffractive light modes due to their inherent geometry. This dual resonant system can lead to an interesting coupling phenomenon. As the plasmonic particles are driven by incident light, two resonances are observed. The first resonance is symmetric and corresponds to the plasmonic resonance of the system and the second resonance occurs as the plasmonic particle is driven close to the eigenfrequency of the secondary resonant system. For an array, the eigenfrequency would correspond to diffractive scattered modes from the lattice spacing. Incident light corresponding to the lattice spacing suppresses the plasmon amplitude because of destructive interference between the incident light and scattered light from the array. An asymmetric Fano resonant

profile is therefore observed where extinction is zero at the lattice spacing and at a slightly lower energy is non-zero.<sup>33,34,35</sup> These strong dipolar interactions can provide diffractive enhancements for surface enhanced Raman scattering<sup>36</sup> and the Fano resonant response can be predictably modulated by changing the lattice constant, geometry of the nanoparticles, and particle composition.<sup>30,33,34,37-43</sup>

### **2.3 Disordered Nanoparticle Lattices**

In recent years, arrays of nanoparticles exhibiting disorder have seen much more attention due to their unique optical characteristics.<sup>44</sup> This class of material could also potentially offer unique insights into emergent phenomena by providing information on how systems moving from disordered to ordered states effect optical resonances.<sup>45</sup> In current literature, the term disorder is mainly used to mean slight variations in the position of particles and amorphous means randomly distributed particles. It is important to note that the average number density is constant, however, in the studies. To understand how disorder effects the resonant response of the array, Albooyeh et al. developed a unique analytical model that would probe these effects.<sup>45</sup> With the model, they were able to calculate the scattering properties for disordered (amorphous) arrays. Experimentally, they created ordered, disordered, and amorphous arrays of double-cut wire pairs of gold/magnesium oxide/gold (Au/MgO/Au) and found good agreement with their model. Helgert et al. went one step further in the definition of disorder and create two classes: isotropic and anisotropic disorder.<sup>46</sup> Isotropic disorder is two-dimensional disorder where particles can have positional variations in both the x- and y-axis in the array. Anisotropic disorder is the one-dimensional analogue of isotropic disorder. They found that these two different types of disorder effect the optical responses differently where the dipole resonance of

the system is highly degraded by polarization in anisotropic systems.<sup>46</sup> Other groups have found similar degradations of the plasmon in disordered systems.<sup>47-50</sup>

One study by Auguie et al. determined that as disorder is increased, the coupled lattice resonance degrades drastically and its lineshape broadens.<sup>50</sup> Miroshnichenko et al. theoretically studied a different type of “disorder” in the system. In the study, individual particles were selectively removed from an ordered array to create an “N-sided defect array” and exact solutions were found for transmission waves.<sup>44</sup>

All of the above studies are unique to disordered systems and provide great insight into the behavior of these systems, however, evaluation of random local perturbations on near-field or aggregate far-field coupled lattice resonances (CLR) has yet to be determined. The aim of this research was to define a new system of disorder referred to as “sparsity” and study the effects on CLR and lattice plasmon resonance (LPR). In particular, the effects of number of particles, referred to as optically active nodes, in the field of view (FOV) and the resulting change to the LPR and CLR will be provided. Statistical data showing the minimum number of optically active nodes required to show CLR were also studied which has not yet been done in the literature. This could provide information on emergent behaviors for nanoplasmonic array systems.

## **2.4 Fano Resonance**

The mathematical description of Fano resonance was first formulated by Italian-American physicist Ugo Fano in his influential 1935 paper titled “Sullo spettro di assorbimento dei gas nobili presso il limite dello spettro d’arco,” which he later translated into English in 1961.<sup>51,52</sup> Fano resonance describes the coupling between a broadband resonance and a discrete resonance; the resulting excitation spectra exhibits an anti-symmetric profile. An example of this

phenomenon is the interference of discrete autoionization states with a continuum in noble gases.<sup>52</sup> Since this type of resonance is a coupled, scattering wave phenomenon, the anti-symmetric excitation spectra can be seen in many different areas of physics and engineering. One particular area of interest is coupled lattice resonance in arrays of plasmonic nanoparticles.

#### ***2.4.1 Classical Analogy to Fano Resonance***

This section will discuss a classical approach of a weakly coupled two-particle system established by Joe et al.<sup>53</sup> which provides a mathematical analogy that gives rise to a Fano resonant profile. The goal is to help guide the understanding of this coupled scattering phenomenon using classical tools.

Begin by considering two particles weakly coupled via a spring, as seen in Figure 2.2, with particle  $\omega_1$  being driven by an external, periodic force. The general equations of motion for the two particles can be written as:

$$\ddot{x}_1 + \gamma_1 \dot{x}_1 + \omega_1^2 x_1 + v_{12} x_2 = a_1 e^{i\omega t} \quad (2.1)$$

$$\ddot{x}_2 + \gamma_2 \dot{x}_2 + \omega_2^2 x_2 + v_{12} x_1 = 0 \quad (2.2)$$

where  $\omega_1$  and  $\omega_2$  are the natural frequencies (eigenmodes) of particles one and two, respectively;  $\gamma_1$  and  $\gamma_2$  are linear damping coefficients of particles one and two, respectively;  $v_{12}$  describes the coupling of the particles,  $a_1$  is the amplitude of the external driving force, and  $\omega$  is the external driving frequency. The coupled eigenmodes are given by:

$$\bar{\omega}_1^2 \approx \omega_1^2 - \frac{v_{12}^2}{\omega_2^2 - \omega_1^2} \quad (2.3)$$

$$\bar{\omega}_2^2 \approx \omega_2^2 + \frac{v_{12}^2}{\omega_2^2 - \omega_1^2} \quad (2.4)$$

where  $\bar{\omega}_1$  and  $\bar{\omega}_2$  are the shifted eigenmodes due to the coupling between particle one and particle two. Only steady state motion of Equations 2.1 and 2.2 will be considered.

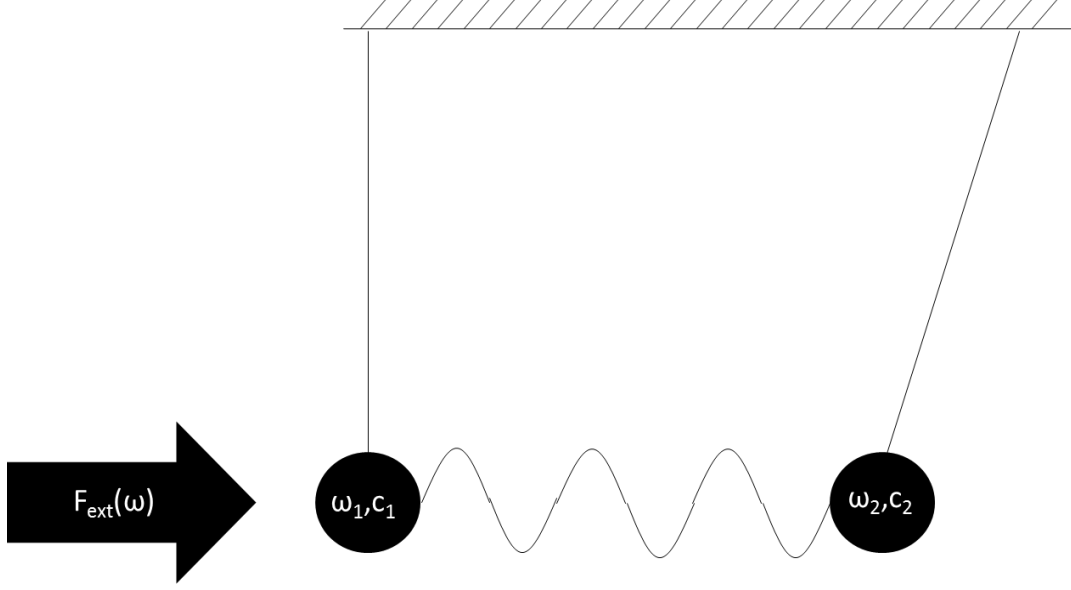


Figure 2.2. Schematic of two weakly coupled particles.

Amplitudes for the particles from the steady state harmonic solutions from Equation 2.1 and Equation 2.2 are found to be:

$$c_1 = \frac{\omega_2^2 - \omega^2 + i\gamma_2\omega}{(\omega_1^2 - \omega^2 + i\gamma_1\omega)(\omega_2^2 - \omega^2 + i\gamma_2\omega) - v_{12}^2} a_1, \quad (2.5)$$

$$c_2 = \frac{v_{12}}{(\omega_1^2 - \omega^2 + i\gamma_1\omega)(\omega_2^2 - \omega^2 + i\gamma_2\omega) - v_{12}^2} a_1, \quad (2.6)$$

where  $c_1$ , and  $c_2$  are the steady state amplitudes for particles one and two, respectively.

The phases of the two oscillators are defined by:

$$c_1(\omega) = |c_1(\omega)|e^{-i\varphi_1(\omega)}, \quad (2.7)$$

$$c_2(\omega) = |c_2(\omega)|e^{-i\varphi_2(\omega)} \quad (2.8)$$

where the phase difference and phase shift are given as:

$$\varphi_2 - \varphi_1 = \pi - \theta, \quad (2.9)$$

$$\theta = \tan^{-1} \left( \frac{\gamma_2 \omega}{\omega_2^2 - \omega^2} \right). \quad (2.10)$$

As a simplistic case, consider the second particle's frictional parameter  $\gamma_2$  to be zero. With this assumption, it is easy to see that in Equation 2.5 the amplitude of the first particle will reach zero as the external force sweeps toward the natural frequency of the second oscillator ( $\omega_2$ ). This is referred to as the zero-frequency and it is the reason for the anti-symmetric profile. The locations of the resonant peaks of the system are approximated in Equation 2.3 and Equation 2.4. Their exact solutions are determined from the real part of the denominator of Equations 2.5 and 2.6 when it is equal to zero. The physical meaning behind the zero amplitude for the first particle can be extrapolated by examining the phases of the two particles. As the external force approaches the first resonance  $\bar{\omega}_1$ , the particle displacement will gain a  $\pi/2$  phase and the amplitude will grow quickly.<sup>39</sup> Right before the external force approaches the zero-frequency, the first particle will be  $\pi$  out of phase with respect to the external force. At the zero-frequency, the phase drops by  $\pi$  very suddenly and as the external force sweeps through the second coupled resonance of the system that phase is gained back. The phase for the second particle at the zero-frequency is shown to be out of phase with the first particle and, as such, leads to a destructive interference at the zero-frequency.

In the more general case where  $\gamma_2$  is not assumed to be zero, the first particle's amplitude does not drop to zero and retains a finite value because of the damping effects in the system. Peak amplitudes of the particles will decrease due to the extra damping in the system and the lineshape will broaden. As the number of coupled particles increases, the position of the zero-frequency is shifted due to the interactions of the particles. If the natural frequency of the coupled particle ( $\omega_2$ ) is lower energy than the driven particle, there is a blue-shift in energy of

the driven particle. An increased number of particles in the system means there is an increase in interactions between them and the driven particle which causes the blue-shift, while the resonance of the coupled particles will red-shift.

#### **2.4.2 Parameter-free Model for Fano Resonance in Plasmonic Structures**

A classical analogy has been presented to help the reader to easily understand Fano resonance. This section will provide another model in the context of plasmonic nanostructures adapted by Giannini et al.<sup>40,54</sup> The main goal of the model is to consider the plasmonic resonance in the Fano model, instead of the flat continuum as was previously explored by Fano, to elucidate the role that the width and energy of the plasmon resonance has on the profile. The derivation of the model makes use of quantum mechanics. Full derivations will be left out and instead the reader is suggested to seek out the works by Giannini for the full derivations.<sup>40,54</sup> In Figure 2.3, a schematic is provided to help with the understanding of how Giannini's model works. Incident light,  $|i\rangle$ , has a probability,  $w$ , to excite a discrete state  $|d\rangle$ . It also has a probability,  $g$ , to excite the plasmonic resonance  $|c\rangle$ , which is the broadband resonance, or quasi-continuum. There exists a small probability,  $v$ , that the discrete state will couple with the plasmonic broadband state.

Fano found in his work that the probability ratio for coupling between a broadband state and a discrete state is:<sup>37</sup>

$$\sigma(\varepsilon) = \frac{(\varepsilon + q)^2}{\varepsilon^2 + 1} \quad (2.11)$$

where  $q$  is the shape parameter determining the asymmetry,  $\varepsilon$  is the reduced energy which depends on the incident photon energy  $E$ , energy of the discrete state  $E_d$ , and the width of the discrete state  $\Gamma_d$ . The reduced energy equation is defined as:

$$\varepsilon = \frac{2(E - E_d)}{\Gamma_d}. \quad (2.12)$$

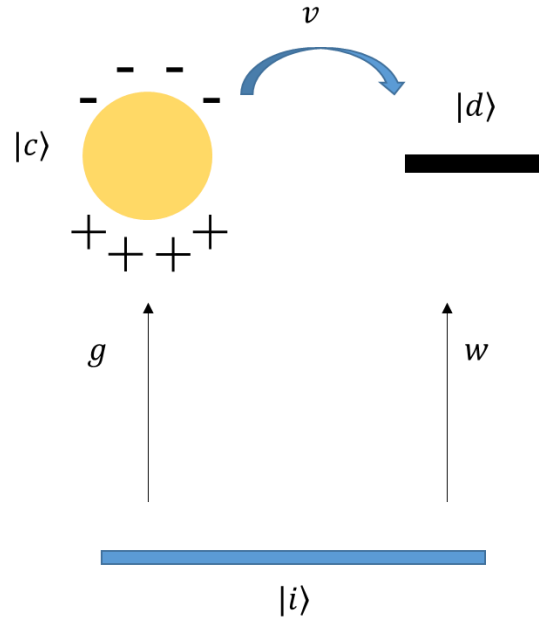


Figure 2.3. Mechanism for broadband plasmonic coupling by incident light.

These two equations do not, however, have any features useful for plasmon resonance. This is overcome by considering the excitation of a plasmon resonance as the governing force that couples the discrete state to the broadband continuum. The goal now is to derive a Fano profile that includes information about the plasmon resonance and discrete resonance.

Consider an unperturbed Hamiltonian function  $\mathcal{H}_0$  with a discrete state  $|d\rangle$  having eigenvalue  $E_d$ , and a broadband continuum state  $|c\rangle$  with eigenvalues  $E$ . A coupling Hamiltonian  $V$  is assumed to couple the discrete state with the continuum state. The matrix elements of the two Hamiltonians are given by:

$$\langle d|\mathcal{H}_0|d\rangle = E_d = 0, \quad (2.13)$$

$$\langle c|\mathcal{H}_0|c'\rangle = E\delta(E - E'), \quad (2.14)$$

$$\langle c|V|d\rangle = v\sqrt{\mathcal{L}(E)}. \quad (2.15)$$

The origin was chosen to be at the discrete energy state, so  $E_d = 0$ .  $|c\rangle$  and  $|c'\rangle$  are different states in the broadband continuum with their corresponding energies  $E$  and  $E'$ .  $\mathcal{L}(E)$  represents the plasmonic line-shape and  $v$  is the coupling factor. The plasmonic line-shape has a Lorentzian form defined as:

$$\mathcal{L}(E) = \frac{1}{1 + \left(\frac{E - E_p}{\frac{\Gamma_p}{2}}\right)^2} \quad (2.16)$$

where  $E_p$  is the position of the plasmonic resonance and  $\Gamma_p$  is the width of the resonance.

With these assumptions, the first step in solving the probabilities of the system is to solve the eigenvalue equation  $\mathcal{H}|\Psi\rangle = E|\Psi\rangle$ .  $|\Psi\rangle$  is the mixed quasi-continuum state and  $\mathcal{H} = \mathcal{H}_0 + V$  is the total Hamiltonian. The next step is to consider an incident photon that is coupled by the Hamiltonian  $W$  to  $|c\rangle$  and  $|d\rangle$  such that the following identities are obtained:

$$\langle i|W|d\rangle = w, \quad (2.17)$$

$$\langle i|W|c\rangle = g\sqrt{\mathcal{L}(E)}, \quad (2.18)$$

where  $w$  and  $g$  are the coupling factors of incident light to the discrete state and quasi-continuum state, respectively. Lastly, the probability that an incident photon excites the quasi-continuum state is found and normalized to the probability of a continuum being excited in the absence of a discrete state (i.e. exciting the plasmon resonance only).

The result is a Fano profile defined in Equation 2.19 through Equation 2.21 that is in terms of the plasmonic energy of the system and the shape parameter.

$$\frac{|\langle i|W|\Psi\rangle|^2}{|\langle i|W|c\rangle|^2} = \frac{(\mathcal{E} + q)^2}{\mathcal{E}^2 + 1}, \quad (2.19)$$

$$q = \frac{vw/g}{\Gamma_d(E)/2} + \frac{E - E_p}{\Gamma_p/2}, \quad (2.20)$$

$$\mathcal{E} = \frac{E}{\Gamma_d(E)/2} - \frac{E - E_p}{\Gamma_p/2}. \quad (2.21)$$

The shape parameter,  $q$ , of the system includes the energy of the plasmonic resonance, width of the plasmonic resonance, the width of the discrete state resonance, and the coupling parameters. A new reduced energy has been defined which is in terms of both the discrete state resonance width and plasmon resonance width as well as the energy of incident light and the plasmon resonance energy value. The discrete state energy width is determined by:

$$\Gamma_d(E) = 2\pi v^2 \mathcal{L}(E). \quad (2.22)$$

In the original Fano model the shape parameter and reduced energy were constant, but now they depend on the coupling factors, energy widths, and energies of the resonances. This implies that there are many different degrees of asymmetry that can be attained depending on the physical makeup of the plasmonic system as well as its geometrical configuration.

## 2.5 Mie Theory

In 1908, a paper written by Gustav Mie was published and would become one of the most influential journal articles on the topic of light scattering.<sup>55</sup> How light interacted with small spheres was not well known in the early 20<sup>th</sup> century which is why this article was so pivotal in understanding of these phenomena. Mie performed a rigorous calculation of light's interactions with sub-wavelength particles and particles whose size was equal to wavelength of light. This allowed for an understanding on scattering and absorption of light by a spherical particle, the polarization, and the color of gold colloids.<sup>55,56</sup> Because there were no computers in 1908, all calculations were performed by hand, and as such, only the first three terms of the infinite series

were considered when solving for the optical cross sections.<sup>56</sup> Modern computers are able to solve the optical cross sections for spheres of arbitrary shape using models such as discrete dipole approximation (DDA), finite-difference time domain (FDTD), and T-matrix theory to name a few.<sup>56</sup>

In Mie theory, the cross sections for scattering, absorption, and extinction for spherical particles is given by:<sup>57</sup>

$$\sigma_x = \pi a^2 Q_x \quad (2.23)$$

where  $a$  is the radius of the particle,  $Q$  is the efficiency, and the subscript  $x$  is used to denote scattering, absorption, or extinction. Scattering efficiency is defined as:

$$Q_{scat} = \frac{2}{q^2} \sum_{\alpha=1}^{\infty} (2\alpha + 1)[|a_{\alpha}|^2 + |b_{\alpha}|^2]. \quad (2.24)$$

The electric and magnetic amplitudes are given by  $a_{\alpha}$ , and  $b_{\alpha}$ , respectively. They depend on dielectric permittivity  $\epsilon$  and magnetic permeability  $\mu$ , as well as the shape parameter. The shape parameter is given by:

$$q = \frac{\omega a}{c} \quad (2.25)$$

where  $\omega$  is the frequency of incident light and  $c$  is the vacuum speed of light.

The scattering amplitudes are:

$$a_{\alpha} = \frac{\mathfrak{R}_{\alpha}^{(a)}}{\mathfrak{R}_{\alpha}^{(a)} + i\mathfrak{I}_{\alpha}^{(a)}}, \quad (2.26)$$

$$b_{\alpha} = \frac{\mathfrak{R}_{\alpha}^{(b)}}{\mathfrak{R}_{\alpha}^{(b)} + i\mathfrak{I}_{\alpha}^{(b)}}. \quad (2.27)$$

$\mathfrak{R}$  and  $\mathfrak{I}$  are functions expressed as spherical Bessel and Neumann functions. Suppose now that  $q \ll 1$  (particles smaller than 100 nm) and the particle of interest is not magnetic, the scattering

efficiency takes on the form for Rayleigh scattering. The formula for Rayleigh scattering holds for negative and positive  $\epsilon$ , except for when the plasmon resonance occurs at  $\epsilon = -2$  as seen in Equation 2.28.

$$Q_{scat} \cong \frac{8}{3} \left| \frac{\epsilon - 1}{\epsilon + 2} \right|^2 q^4 \quad (2.28)$$

Extinction of light by gold colloids was studied by Mie<sup>55</sup> where for particles around 80 nm a maximum of 525 nm was calculated. Particles between 100 nm and 180 nm had a maximum extinction around 550 nm but would decrease in magnitude.<sup>56</sup> These findings were some of the earliest representations of plasmonic dipoles in gold colloidal suspensions and Mie's calculations are still used to help form a theoretical foundation for plasmonic behavior in metallic nanoparticles.

Figure 2.4 is presented as an example comparing Mie calculations with one of the experimental spectrum of a two-dimensional sparse array created for this research. A 76 nm diameter particle with a coating of refractive index 1.527 and a medium refractive index of 1.421 was used for the Mie theory calculation to match the polyvinylpyrrolidone (PVP) coated gold nanoparticles and medium used for the sparse arrays in this research. The PVP shell size was 10 nm.<sup>58</sup>

The single particle Mie calculation of the plasmon has a maximum extinction around 570 nm whereas, for the fabricated sparse array, the plasmon occurs around 550 nm. This 20 nm blue-shift in the plasmonic response is due intrinsically because of the array configuration as well as the coupling between gold nodal elements in the array. A blue-shift of the plasmon is in good agreement with the classical analogy of Fano resonance. When two plasmonic nodal elements are coupled together, the system will exhibit a coupled eigenmode resonant frequency that is different than the single nodal element eigenmode. The blue-shift in the plasmonic

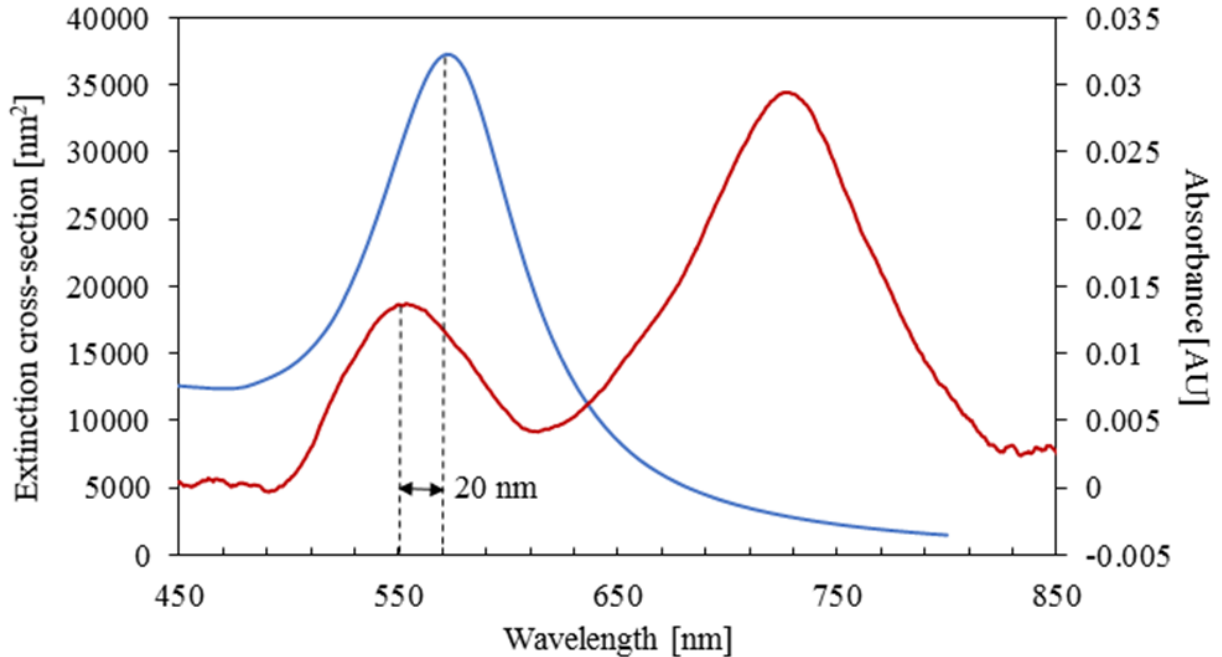


Figure 2.4. Single particle Mie theory comparison with experimental data. A 76 nm gold nanoparticle with a PVP shell of 10 nm and refractive index of 1.527 in a medium of refractive index 1.421 (blue data) is compared with an experimentally fabricated two-dimensional array with 13,223 gold nodal elements having the same particle and medium parameters (red data).<sup>58</sup>

resonance is in part due to in-plane scattering of light whose wavelengths are near and/or at the size of the lattice spacing. In-plane scattered light with these wavelength values will interfere with the ability of the plasmon to be excited. Thus, it takes more energy to excite the plasmonic resonant mode for the array.

## 2.6 Summary

Metamaterials offer unique characteristics that could be used in many areas of engineering and the sciences such as thermal energy harvesting, solar cells, and chemical sensors to name a few. Plasmonic metamaterials allow for the manipulation of electromagnetic radiation at sub-wavelength dimensions. Plasmons are defined as the coherent oscillations of the electron gas in the metal nanoparticle. When ordered in an array with lattice spacing commensurate with

the wavelength of light, a coupling can occur between the plasmonic mode of the array and in-plane diffracted light. This coupling is referred to as the coupled lattice resonance (CLR). For perfect systems, the coupling has a characteristic antisymmetric Fano resonant line shape where a complete destructive interference will cause the spectral magnitude to decrease to zero.

However, there remains a finite value for systems that incorporate dampening. Disorder in the array has been shown to decrease the magnitudes of the resonances in these types of systems as well as broaden both the plasmonic resonance and the CLR. A parameter-free description has been identified to elucidate how the plasmonic activity effects the Fano resonance of the system.

## Chapter 3 - Fabrication and Characterization of Two-Dimensional Arrays

Throughout the years in scientific literature, there have been many methods used for creating homogeneously ordered 2D arrays of metallic nanoparticles. Each method has benefits and drawbacks and this chapter will be focused on highlighting, briefly, those different methods and provide the experimental design for fabricating arrays using the block copolymer poly(dimethylsiloxane-b-ethylene oxide).<sup>59</sup>

### 3.1 Fabrication Methods

Homogeneously ordered, and sparse arrays are obtainable via different methods including: electron beam lithography (EBL)<sup>60</sup>, nanoimprint lithography (NIL)<sup>61</sup>, nanosphere lithography (NSL)<sup>62</sup>, and focused ion beam systems (FIB).<sup>63</sup> These systems are able to produce extremely precise arrays of nanoparticles with tunable geometries, periodicities, and particle size. However, some require expensive machinery, highly trained personnel, etching, deposition, etc. Electron beam lithography utilizes a polymeric resist and an electron beam to create complex patterns defined by the user. The throughput of single beam machines, however, tend to be limited and equipment can cost in the millions of dollars. With NIL, high throughput is possible but surface deformations can occur. For this method, a pattern is created on a “master stamp” by an electron/ion beam and is used to mold the pattern onto a substrate via a resist. NSL also can have high throughput but deformations and dislocations tend to reduce fidelity of the array. This is, in part, because the method relies on deposition of colloidal spheres as a mask to control the pitch of the array. In FIB, gallium ion beams mill the substrates to create patterns with high precision but can be costly and limited to single-beam throughput. For this project, a template-based self-

assembly method was chosen which makes use of soft lithography because of ease of fabrication and low cost. Table 3.1 summarizes all of these methods.

In recent years, template-based self-assembly has been gaining favor as a method for creating 2D arrays of metallic nanoparticles because of its economic viability, and its advantage over regular self-assembly. Deposition by regular self-assembly is dependent on interfacial forces between particle, solution, and substrate, and forces between each particle. Complex patterns are therefore difficult to obtain. Template-based self-assembly remedies this problem by allowing for control of assemblies due to topographical patterning that directs particles toward the periodic centers. Templated substrates have been studied with processes involving electrostatic and magnetic forces, convective flows, capillary forces, sedimentation, etc. and in particular those processes involving capillary and convective forces have gained popularity.<sup>64-72</sup> Substrates used in these processes include polydimethylsiloxane (PDMS), SiO<sub>x</sub>, and mylar films.

Table 3.1. Summary of common methods to obtain arrays of nanostructures.

Method	Substrate	Area	Comments
EBL	Electron beam patterns a polymeric resist	μm <sup>2</sup>	<ul style="list-style-type: none"> <li>• ~\$1-2 million in cost</li> <li>• low throughput</li> <li>• well characterized</li> <li>• complex patterns possible</li> </ul>
FIB	Ga ion beams used to mill into substrates or deposit metals/insulators onto substrates	μm <sup>2</sup>	<ul style="list-style-type: none"> <li>• ultra-smooth metal films possible</li> <li>• defects and interstitials lead to unwanted amorphous layers</li> <li>• Ga doping of sample</li> </ul>
NSL	Colloidal crystal spheres mask areas of substrate during metallization	μm <sup>2</sup>	<ul style="list-style-type: none"> <li>• high throughput</li> <li>• reproducible and facile</li> <li>• tunable particle diameters; limited geometries</li> <li>• dislocations and defects can be present</li> <li>• limited to hexagonal arrays</li> </ul>
NIL	Stamp patterns are molded onto substrates using resists	cm <sup>2</sup>	<ul style="list-style-type: none"> <li>• low cost</li> <li>• high throughput</li> <li>• short fabrication time</li> <li>• possible mechanical deformations of surfaces</li> </ul>

### 3.2 Soft Lithography and Poly(dimethylsiloxane-b-ethylene oxide)

Soft lithography was the fabrication process of choice in the present work for making stamps to order gold nanoparticles into because it is a simple process, scalable, does not employ harsh/dangerous chemicals, does not require expensive machinery to make the array, and is a cheap process. This technique involves a pre-lithographed stamp referred to as the “master stamp” which is used to create a negative imprint of its pattern in a polymer substrate.<sup>64,65,69</sup>

The polymer most widely used for this technique is PDMS due to its ability to very precisely conform to a patterned substrate. PDMS is also optically transparent which makes it very useful in optoelectronic systems. However, it has a surface free energy of 20 mN/m<sup>73</sup> which is small when compared to water (72 mN/m<sup>74</sup>). This low surface free energy necessitates modifications to the substrate in order to be useful for applications such as microfluidics. Several methods such as oxygen plasma, sol-gel coatings, plasma processing, etc. can be used to modify the PDMS surface and make it hydrophilic.<sup>64,65,75,76</sup> However, because of PDMS’s low glass transition temperature of -120 °C, it does not remain hydrophilic for long ( $\leq 4$  hours).

In the present work, poly(dimethylsiloxane-b-ethylene oxide) (PDMS-b-PEO) block copolymer was used to rapidly render PDMS stamps hydrophilic by simply mixing the copolymer, base PDMS, and curing agent together and curing. Yao et al. reported that by increasing the concentration of PDMS-b-PEO, the water contact angle decreased roughly five-fold.<sup>77</sup> Wetting properties of PDMS can also be impacted by the cross-linking density.<sup>78</sup> Using the block copolymer in this way is unique because it will allow the stamp to remain hydrophilic for up to 20 days.<sup>77</sup> These properties and its low cost make it a great hydrophilization method of PDMS to obtain 2D arrays of particles. It is the author’s understanding that there is no current

literature on obtaining 2D arrays using the block copolymer, making it a unique and interesting avenue to explore.

### **3.2 Materials and Equipment**

A silicon stamp was purchased from Lightsmyth Technologies (Eugene, OR, USA) to be used as the master stamp with a post spacing of 700 nm, 350 nm height, and 260 nm diameter. A hot plate (#090921001) and soda lime microscope glass slides were obtained from VWR (Philadelphia, PA, USA). PDMS was obtained in a kit from Dow Corning Corporation (Midland, MI, USA). A block copolymer poly(dimethylsiloxane-*b*-ethylene oxide) (PDMS-*b*-PEO) was obtained from Polyscience Inc. (Warrington, PA, USA) to render the PDMS stamp hydrophilic. Speed mixer purchased from Flack Tek Inc. (Landrum SC, USA) was used to thoroughly mix PDMS with PDMS-*b*-PEO and curing agent. A Nikon light microscope (Eclipse LV100 D-U) was purchased from Nikon (Melville, NY, USA) and used for diascope and episcopic illumination. Andor Spectrum Analyzer (Shamrock 303) was purchased from Andor Technology (Belfast, UK) and attached to the Nikon microscope to obtain spectra of samples through diascope and episcopic illumination. Spectrum analyzer has a variable entrance slit width where 200  $\mu\text{m}$  was chosen. MATLAB R2016a (Mathworks, Natick, MA, USA) and ImageJ (National Institutes of Health, Bethesda, MD, USA) were used to analyze images of the sample obtained in diascope and episcopic illumination.

### **3.3 Stamp Fabrication and Particle Deposition**

The PDMS-PEO mixture was prepared by combining base PDMS, curing agent, and PDMS-*b*-PEO in a ratio of 100:10:2.07 by mass into a plastic Flack Tek container and speed

mixed at 3000 rpm for six minutes. Approximately 70 mg of this prepolymer mixture was dropped on to the silicon master stamp and another drop was placed onto a clean glass slide (refer to Figure 3.1). The master stamp with the prepolymer mixture was then overturned onto the mixture on the glass slide and placed in a vacuum desiccator at 30 inches Hg to remove bubbles. Once all bubbles were removed via successive pressurizing/depressurizing in the vacuum desiccator, the construct was placed on a hot plate at 100 °C for two hours. Once cured, the PDMS-PEO stamp could be easily removed from the silicon master stamp using tweezers and stored in plastic containers. Because the silicon master stamp had posts, the resulting PDMS-PEO stamp would form cylindrical cavities.

Concentration of AuNPs for deposition was determined based on a calculation of the total number of cavities in the PDMS-PEO stamp. Dried gold nanospheres (76 nm, poly(vinylpyrrolidone) (PVP) capped) were purchased from Nanocomposix (San Diego, CA, USA). The powder was approximately 15% Au and 85% PVP by mass.

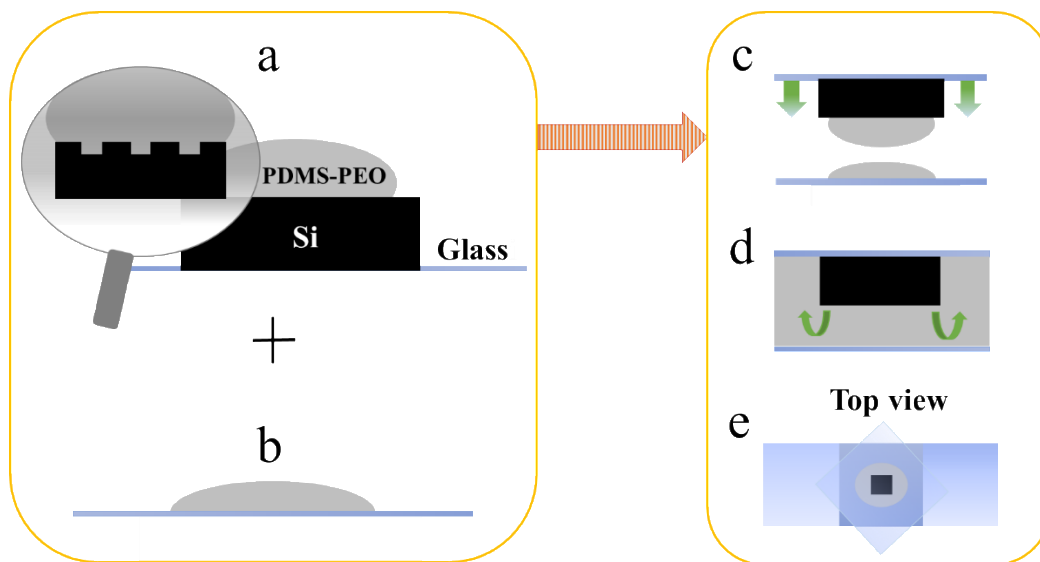


Figure 3.1. Fabrication of nanopatterned PDMS-PEO stamp for particle deposition. a) Globule of PDMS-PEO (grey) was dropped onto silicon (Si) stamp (black) on glass (blue), b) PDMS-PEO was dropped onto glass, c) inversion of Si stamp with PDMS-PEO onto glass, d) construct after inversion, e) top view of construct.<sup>59</sup>

To determine the appropriate concentration, consider a 700 nm x 700 nm grid ( $4.9 \times 10^{15}$  nm<sup>2</sup>) which contains four quarters of cavities or one total cavity. This is illustrated in Figure 3.2. The sample area of the nanoimprinted stamp is approximately 0.664 cm<sup>2</sup> and dividing the total sample area by one square grid gives approximately  $1.4 \times 10^8$  cavities.<sup>59</sup>

The AuNP solution was created by mixing approximately 4.21 mg of the NP powder to 3 mL of distilled and deionized water producing approximately 0.21 mg/mL solution of AuNPs. The maximum amount of solution that would fit inside the stamp cavity was 40  $\mu$ L. This would provide a concentration of  $1.9 \times 10^9$  particles. A larger concentration was chosen to ensure that at least one particle was deposited in each post and to account for any problems that could occur during the drying process.<sup>59</sup>

The PDMS-PEO stamp was placed in a distilled and deionized water bath for 60 seconds and dried with N<sub>2</sub> in order to clean any dust from the stamp. A glass microscope slide with a 0.31 cm wide hole drilled into it was cleaned with the same method as above and placed on top of the excess un-patterned PDMS-PEO thereby creating a sealed area for the solution to be added. Forty  $\mu$ L of the AuNP solution was pipetted through the glass hole into the area of the nanopatterned PDMS-PEO stamp. In the upper left hand corner of Figure 3.3 is the PDMS-PEO construct with the glass cover and AuNP solution added. Drying took place over two hours at 25  $^{\circ}$ C.<sup>59</sup>

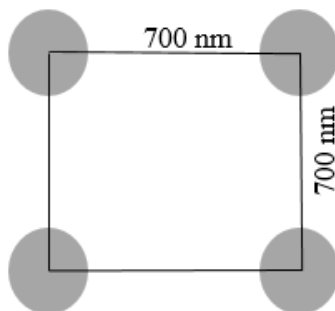


Figure 3.2. Square grid of cavities.<sup>58</sup>

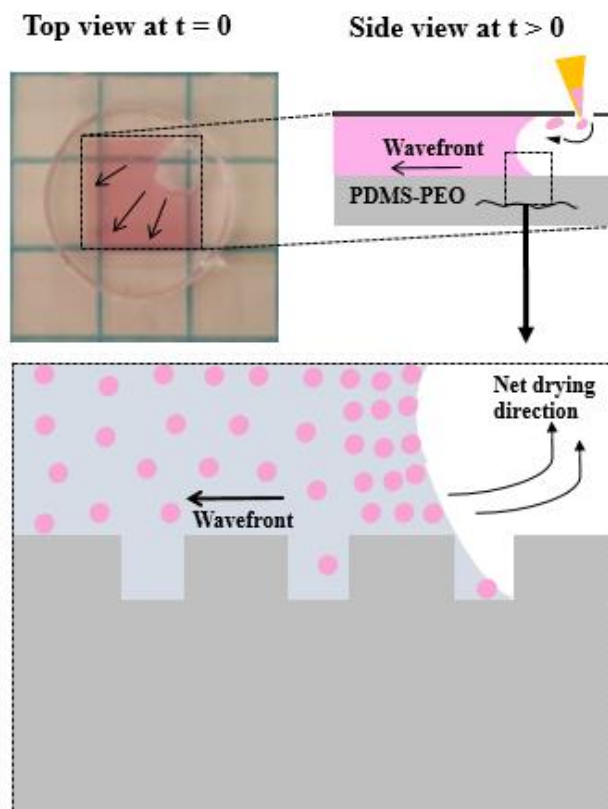


Figure 3.3. Continuous dewetting process of gold nanoparticles into PDMS-PEO stamp. Top left hand corner shows the PDMS-PEO construct with gold solution sandwiched between the glass cover and the stamp. Top right hand corner illustrates how the solution was pipetted into the cavity. Bottom of image proposes the drying/deposition process.<sup>59</sup>

### 3.4 Procedure for Capturing Images and Spectra

After drying was finished, the stamp was characterized using a Nikon microscope with attached spectrum analyzer. A series of images were captured with varying numbers of deposited AuNPs (optically active nodes) by moving the stamp on the microscope stage horizontally and using both a 50x objective and 100x objective. This series of images and spectra spanned less than 10% active nodes in the FOV up to an area greater than 80% active nodes. Each successive image captured was separated by approximately 20 columns for 50x objective and 6 columns for 100x objective images. A smoothing procedure was performed on the spectral data using a

Savitzky-Golay algorithm in MATLAB. Values chosen to perform the smoothing were a polynomial degree of four and an average window of 101 points. Figure 3.4 shows a comparison for data taken with 100x objective in episcopic illumination and corresponds to 1363 optically active nodes.<sup>59</sup>

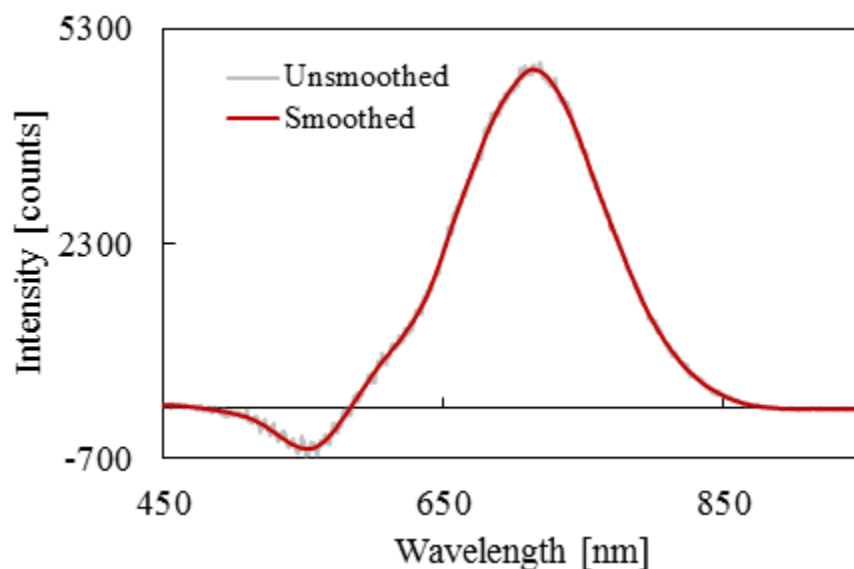


Figure 3.4. Comparison of smoothed and unsmoothed spectra captured in episcopic illumination.<sup>58</sup>

### 3.5 Summary

Arrays of nanoparticles can be fabricated by many methods such as electron beam lithography, nanoimprint lithography, focused ion beam lithography, and nanosphere lithography. Each method of fabrication has advantages and disadvantages; however, this work used a polymer template-based self-assembly technique due to ease of use, and inexpensive fabrication tools. A nanoimprinted master stamp was used to create a patterned polymer substrate using the polymer PDMS. PDMS is a biocompatible polymer that will replicate a patterned surface well. Due to its extreme hydrophobicity, however, the block copolymer PDMS-b-PEO was used to render the stamp hydrophilic. This block copolymer was chosen because it can

simply be added to the base PDMS and mixed in large batches. Other techniques, such as sol-gel coatings, require more time and tools to render the surface of PDMS hydrophilic. Typically, PDMS will keep its hydrophilicity for less than one day using alternative methods, but with PDMS-b-PEO, a PDMS stamp can remain hydrophilic for up to 20 days.

An aqueous gold nanoparticle solution was created with a concentration based on the approximate number of cavities in the PDMS-PEO stamp. Continuous dewetting technique was used to deposit the particles in the nanocavities of the stamp. Episcopic and diascopic microscopy characterization was performed on the fabricated sparse arrays. Dark field images and spectra were obtained for areas with larger amounts of sparsity and areas with decreasing amounts of sparsity.

## **Chapter 4 - Characterization of Sparsely Deposited Gold Nanoparticle Arrays**

By using the block copolymer poly(dimethylsiloxane-b-ethylene oxide) (PDMS-b-PEO), a sparse array with deposited gold nanoparticles (AuNPs) inside cavities, defined as optically active nodes, was obtained. When nanoparticles are ordered, they can couple with other particles in the array to produce an array plasmon (AP) whose response is different than a single nanoparticle. Coupling between nanoparticles supports a spectral feature that is commensurate with the array spacing known as the coupled lattice resonance (CLR).<sup>33-35</sup> Fabricating an array of nanoparticles can be done by various means as previously highlighted, but having the particles couple will depend on the polarizability of the particles, and the homogeneity of deposition. The fabricated samples obtained were non-homogenously ordered where, in a particular field of view, there may have been a number of particles missing in a column of the array. In this chapter, characterization of the fabricated sample done by an all optical method in both diascopic and episodic illumination, statistical data on sparsity, and comparisons of experimental data to simulation and another scientific work will be discussed.

### **4.1 Analysis of Sparse Array Using Diascopic Illumination**

Diascopic illumination, also known as transmission mode microscopy, is a method to obtain spectra and/or images from a sample where the source light shines from under the sample and transmits through the sample, interacts with the sample, and proceeds to the spectra analyzer/image device. Refer to Figure 4.1 for an illustration of the setup used. All diascopic illumination spectra in this experiment were obtained using a 50x magnification objective in bright field mode (BF). All images obtained for analysis were done with a 50x objective under episodic illumination in dark field mode (DF). Images were obtained in this particular mode

because it provided a better contrast image for counting optically active nodes. The aperture size was approximately 200  $\mu\text{m}$  and light was polarized in x-direction.<sup>59</sup>

The sample was placed in a way to have the excess PDMS-b-PEO on two cut pieces of microscope slide on the stage of the microscope as seen in Figure 4.1. A reference 2% PDMS-b-PEO was used for spectra baseline and placed in the same fashion. The purpose of placing the sample and the reference on cut pieces of microscope slide was to raise them off of the glass microscope stage so that only air was contacting them above and below, eliminating any dielectric effects that could change the obtained spectra. To do the analysis on sparsity, an area on the sample was chosen and spectra with a corresponding image were obtained for seven different fields of view (FOV) by moving the stage horizontally into an area with fewer numbers of optically active nodes in the FOV. Figure 4.2 and its inset shows the results obtained.

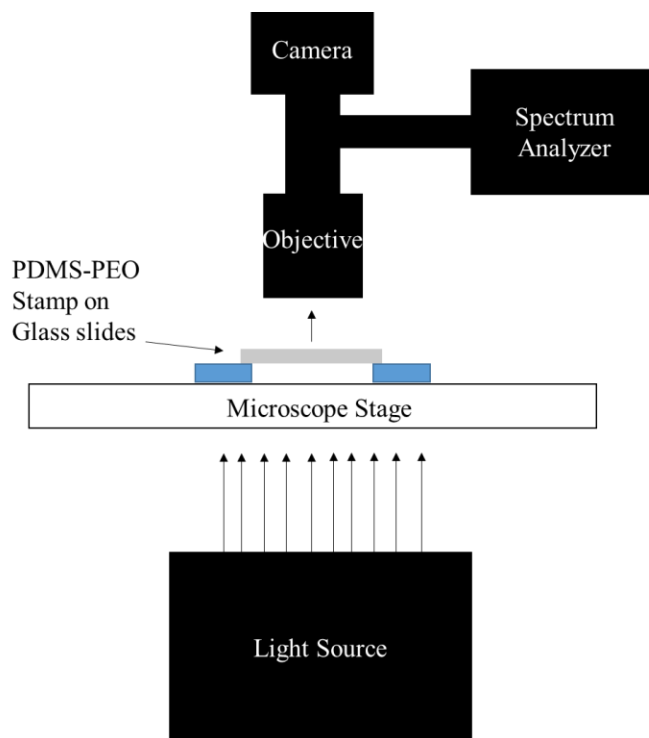


Figure 4.1. Illustration of the setup used for diascopic characterization of the sample. Under diascopic illumination light rays transmit through the sample and interact with the sample. The light passes through the objective and passes through a 50/50 beam splitter for imaging and spectral analysis.

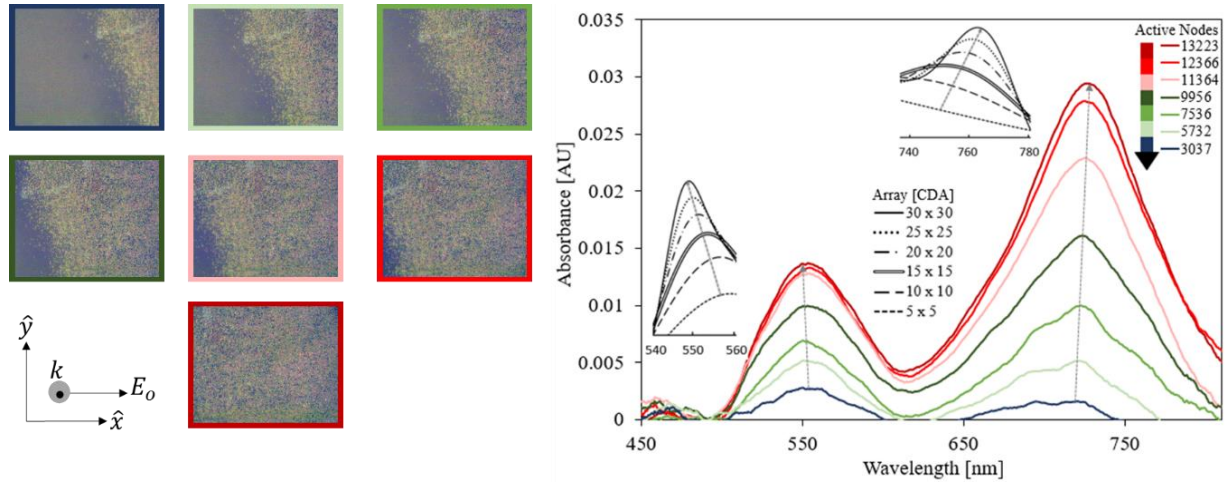


Figure 4.2. Diascopic characterization of AP and CLR features for varying areas of sparsity. DF images captured using 50x objective. Inset shows simulated AP and CLR peak shifts for homogenous arrays of varying particle counts.<sup>59</sup>

In Figure 4.2, the first resonance feature corresponds with the array plasmon which occurs around 555 nm and is blue-shifted from the single nanoparticle Mie theory result discussed in Chapter 2. Blue shifting of the array plasmon resonance from the single nanoparticle response occurs because the array plasmon (broad band resonance) coherently couples with scattered light from the lattice (discrete resonance, 700 nm) causing a shift in their natural frequencies (eigenmodes). The size of the array (i.e. number of optically active nodes) also effects the array plasmon in the same fashion due to coupling between nodes.<sup>59</sup>

The lattice spacing of the fabricated array was 700 nm. Based on the classical analogy provided in Chapter 2, one would expect the zero-wavelength to correspond to 700 nm. However, because there are multiple coupled particles in the array the corresponding dip shifts; the dip in the array was approximately 640 nm. A secondary resonance feature was obtained around 720 nm due to the shift in the natural frequency from coupling between the array plasmon and scattered light. This secondary response was the Fano resonant CLR for the array.

The top left hand inset in Figure 4.2 shows the DF images obtained and the colored perimeter around them corresponds to the optically active nodes that gave the absorbance spectra

(number provided in legend). Number of optically active nodes ranged from 3037 to 13,223 relative to a total of 15,502 nodes possible. In a 50x image the active nodes populate approximately 18% of all active nodes in the aperture window (200  $\mu\text{m}$ ). Extinction magnitudes for the array plasmon increased linearly and blue-shifted as the number of optically active sites increased in the FOV while for the CLR they red-shifted and increased non-linearly. CDA simulations are provided as an inset to simulate extinction peaks of CLR from constructive coupling of AP and diffracted light. Array sizes were varied from 5 x 5 to 30 x 30 with a particle radius of 38 nm and lattice pitch of 700 nm to match the experimental materials. Simulated arrays were homogenous with one particle per node. A unique refractive index,  $n = 1.08$ , was chosen accordingly to match theoretical with experimentally measured resonant wavelengths. AP and CLR features are placed near their corresponding measured counterparts from the sample.

#### **4.2 Analysis of Sparse Array Using Episcopic Illumination**

Episcopic illumination, also known as reflection mode microscopy, is a method to obtain spectra and/or images from a sample where the source light shines from above the sample and interacts with the sample. Reflected light is captured by the spectra analyzer/image device. Refer to Figure 4.3 for an illustration of the setup used. All episcopic illumination spectra in this experiment were obtained using a 100x magnification objective in bright field mode (BF). All images obtained for analysis were done so with a 100x objective under episcopic illumination in dark field mode (DF). The aperture size was approximately 60  $\mu\text{m}$  and light was polarized in x-direction. The characterization was done in the same fashion as with diasopic illumination. Images and spectra were taken at the same spot as in diasopic illumination, however, the difference between the two image sets was the size of the aperture and how the light was

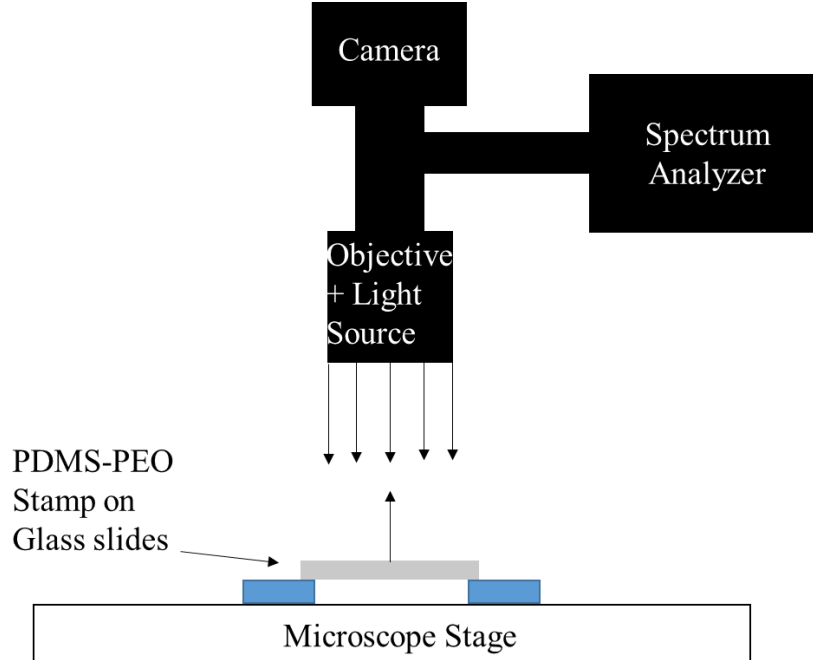


Figure 4.3. Illustration of the setup used for episcopic characterization of the sample. The light source in the Nikon microscope used was physically located behind the objectives. Light passed through filters, aperture, and field stop whereby it finally reached the objective and was focused on the sample.

collected (reflected versus transmitted).

Figure 4.4 shows the results of ten spectra as a function of array sparsity. Each image was captured by moving the stage horizontally and obtaining a new FOV, same as with diasopic mode. The number of optically active nodes ranged from 148 to 1363 relative to a maximum of 1721 nodes. Negative values for AP intensity was due to episcopic illumination because light absorbed or scattered in-plane did not get sent back to the spectra analyzer. A higher initial baseline intensity of the control at the AP wavelength range would subtract from the measured intensity values after the sample was in place, resulting in negative values at the AP wavelength range. Similar to diasopic illumination, the CLR feature red-shifts due to a cumulative constructive interference from scattering and backscattering by neighboring optically active

nodes. On the other hand, the AP blue-shifts when the array size increases due to a higher incident energy compensating for the constructively interfering scattered and backscattered light with a wavelength of 700 nm.<sup>59</sup>

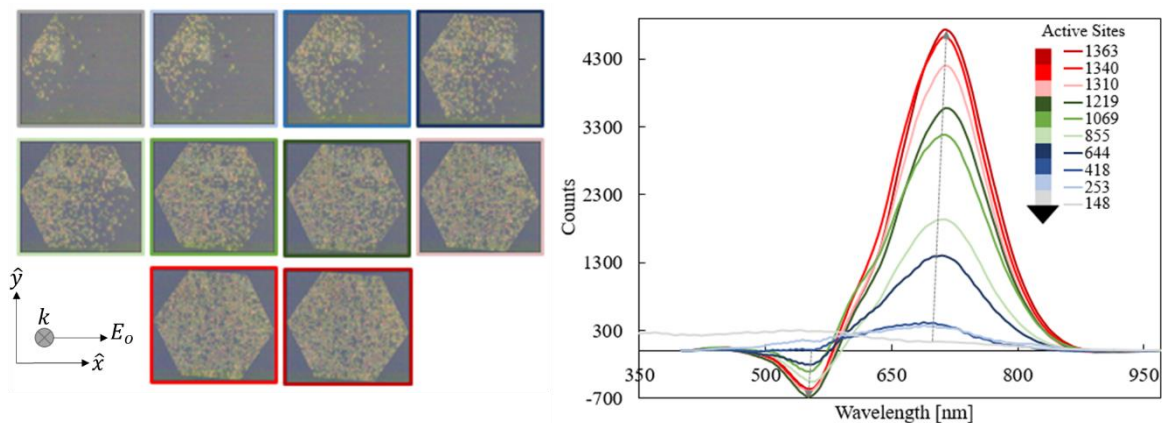


Figure 4.4. Episcopic characterization of AP and CLR features for varying areas of sparsity. DF images captured using a 50x objective.<sup>59</sup>

#### 4.3 *In silico* Analysis of Optically Active Nodes by Use of Photometric Properties of AuNPs

In order to begin to understand how sparsity effects the resonances of an array of nanoparticles, a proper method for counting particles needed to be established. This work refined computational image analysis and removed the need for manual counting of particles in an image by creating a custom subroutine to analyze sparsity in two-dimensional arrays based on computed distribution of inhomogeneity. Current image analysis software provides functions for automated particle/object counting allowing the user to obtain particle/object properties by isolating the particles with respect to the background.<sup>79–82</sup> These tools, however, require high contrast images. For low contrast images, there are correction methods that can be used to enhance the contrast such as thresholding. Episcopic and diasopic images obtained for this thesis contain up to 13,223 closely-packed optically active nodes and are low contrast so using conventional methods for automated counting did not prove useful.

The trichromatic additive color model uses red, blue, and green (RGB) to specify numerical values for each pixel of an image obtained by an image capturing device. In order to efficiently store information and optimize memory, each image capture device applies a non-linear transfer function to the RGB signal and converts the response into non-linear R'G'B' values.<sup>83,84</sup> Photometric luminance of an image is a combination of these non-linear values and is defined as the luma of the image and is mathematically obtained by:

$$Y' = 0.299R' + 0.587 G' + 0.114B' \quad (4.1)$$

Most image analysis packages such as Adobe, GIMP, and MATLAB have protocols for determining the luma of an image based on Equation 4.1 for every pixel in the image. A MATLAB subroutine was written as an alternative method for counting optically active nodes in images obtained in the current work by finding the mean luma values for each node and thresholding with the overall luma in the image.

Manual counts were first obtained from the images shown in Figure 4.2 and Figure 4.4 to be used as a reference for writing the MATLAB subroutine for future automation of counting nodes in images. The cell counter plugin from ImageJ software was used to obtain the manual counts. The counter works by assigning a color and number for the user to associate with a particular type of object to count in their image and tallies up the total.

The MATLAB subroutine imported an image obtained from episcopic or diasopic illumination for analysis with the ultimate goal of creating a matrix to count the optically active nodes based on luma. Each image captured had a resolution of 1920 x 2560 pixels but the size of each node was such that a matrix could not be created, so the subroutine resized the image in order to obtain a matrix that incorporated each active node (see Figure 4.5a). Once resized, the subroutine determined the luma of each pixel in the image using Equation 4.1. For 100x images

the size of a node was 34 x 34 pixels and for 50x images the node size was 18 x 18 pixels. Next, the subroutine averaged the luma for all pixels making up a node and stored the value in a matrix which then got converted to binary form based on thresholding. Threshold values were determined based on a sensitivity analysis from manual counts and average luma of the entire image. Threshold values ranged from  $\pm 5$  to 10. A binary value of 1 represented a filled node and 0 represented an empty node. Lastly, the subroutine added up each value of 1 in the matrix and output the result.<sup>59</sup>

Figure 4.5b shows the linear relation between luma and active nodes in a FOV from episcopic (hexagons) and diasopic (filled black squares) images obtained from the subroutine. Figure 4.5c shows how each optically active node was determined by the customized MATLAB subroutine based on trichromatic modeling and luma sampling, and known manual counts. Figure 4.5d plots the frequency of chains containing 1 to 14 optically active nodes for areas containing 148, 1069, and 1363 total optically active nodes in 100x images. Images used can be seen in Figure 4.4.<sup>59</sup>

Applications for chemical sensing and chemical sample differentiation have previously been reported where trichromatic models (RGB) determine photometric characteristics of AuNPs.<sup>85,86</sup> Aluminum nanoclusters exhibiting fano-resonant activity have been fabricated for colorimetric AP sensing using an RGB variant known as xy color space which is defined by the International Commission on Illumination (CIE).<sup>87</sup> The work performed for this thesis correlated the number of active nodes with the strength of CLR and AP signals obtained in different FOVs having different amounts of sparsity in the array and was achieved photometrically by capturing the change in luma of DF images with respect to AuNP population. The need for image correction tools was eliminated by this colorimetric analysis as well as reducing computational

time in demarcating active nodes.

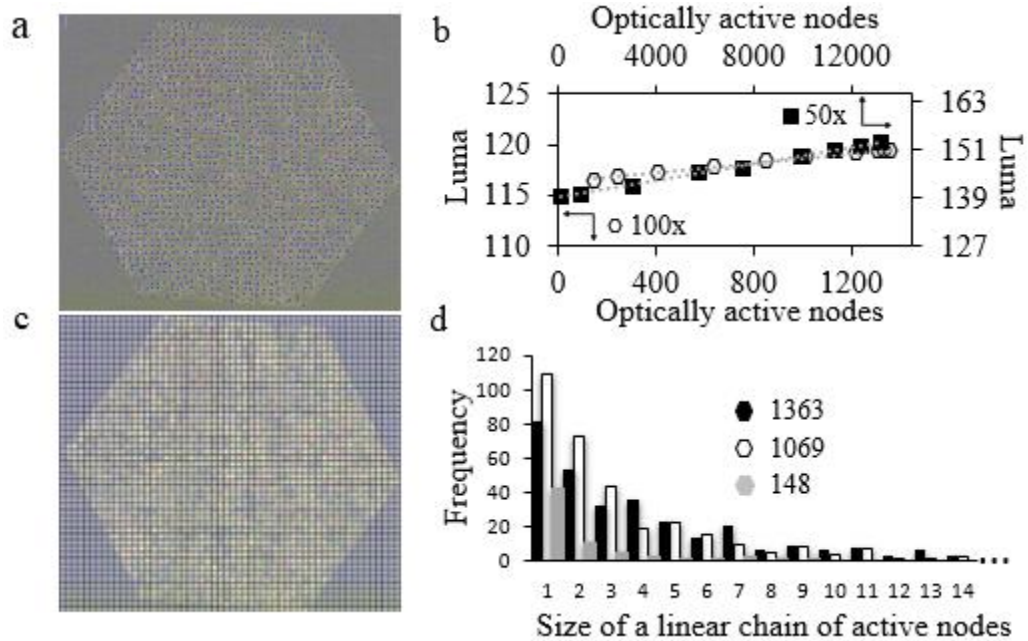


Figure 4.5. Illustration for counting particles manually, and computationally using luma. a) manual counts of active nodes using ImageJ cell counter plugin, b) linear dependence between luma and active nodes for episcopic (hexagons) and diascopic (filled black squares) modes, c) grid used by MATLAB subroutine to determine active nodes based on luma and d) distribution of sizes for 1D chains of active nodes obtained by MATLAB subroutine.<sup>59</sup>

#### 4.4 Particle Chain Size Distribution and Emergence of Fano Resonance

Sparsity in the fabricated array effects the emergent optical features as can be seen in Figure 4.2 and Figure 4.4 by causing a distribution of 1D chains of optically active nodes with varying lengths. Figure 4.6 shows the distribution of chain sizes obtained by using a MATLAB subroutine. The median chain size (labeled red) showed an increase with increasing optically active nodes resulting in a more homogenous and less sparse array.<sup>59</sup>

Emergence of a Fano resonant CLR was found with as few as five optically active nodes on average in a continuous chain. Figure 4.7 shows that this minimum value was important for the emergence of the resonance in the sparse system. The minimum value also provided a

measurable response of the CLR before the array plasmon.

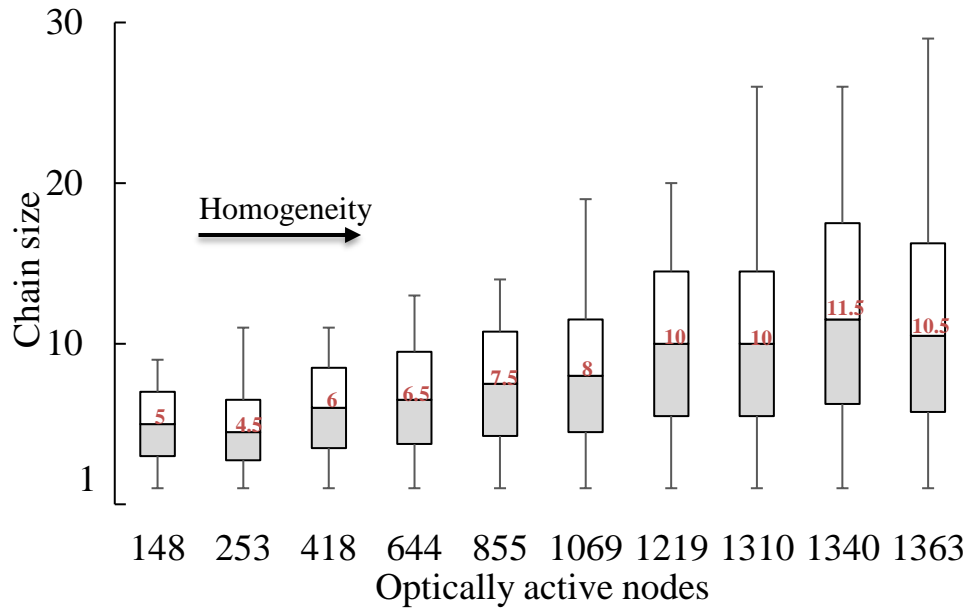


Figure 4.6. Chain size distributions for areas captured in episcopic mode.<sup>59</sup>

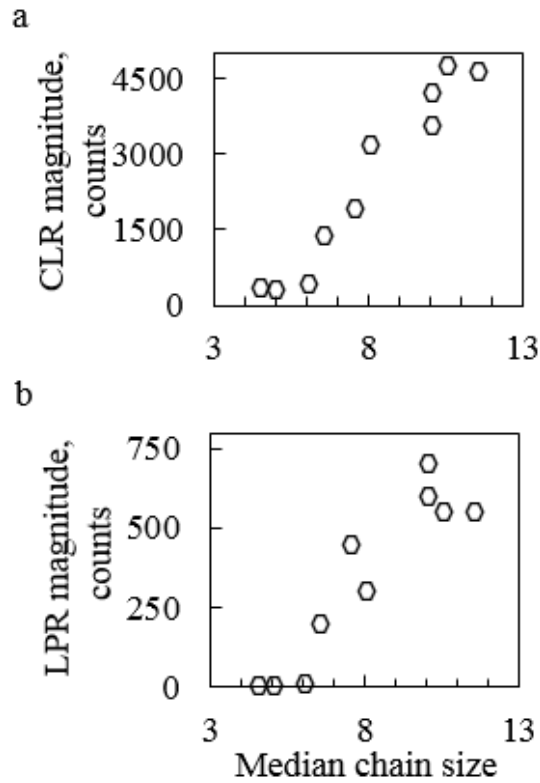


Figure 4.7. Magnitudes of intensity versus median chain size for images captured from episcopic characterization. Larger intensities can be seen with increasing median chain size for a) coupled lattice resonance and b) array plasmon.<sup>59</sup>

In literature, emergence of Fermi liquid features were theoretically obtained computationally using string theory by increasing the fermion density away from the relativistic quantum critical point of the designed system.<sup>88</sup> Reversible changes in optical responses of two-dimensional super-lattices of silver and gold nanoparticles which emerged by small, pressure-induced variations in inter-particle spacing occurring below a critical separation threshold have previously been reported.<sup>10,11</sup> Emergence of unusual composite spin degrees of freedom in magnetically frustrated  $\text{ZnCr}_2\text{O}_4$  due to a finite low-temperature spin correlation length have been studied as well.<sup>8</sup> These examples, along with the analysis of chain sizes in AuNP sparse arrays, suggest that emergent behavior could occur in a system provided a sufficient critical point has been achieved.

The magnitudes of LPR and CLR in Figures 4.2 and 4.4 increased when the median chain size increased beyond the critical point of emergence for the sparse array system. A similar increase in magnitudes of experimental and simulated lattice scattering was previously reported by Auguie and Barnes when positional disorder decreased in two-dimensional arrays of ellipsoidal nanoparticles on Si substrates.<sup>50</sup> However, the magnitudes of the LPR increased with an increase in disorder contrasting with present work; LPR was reported to be approximately half of the CLR feature which is in good agreement with present work as shown in Figure 4.2. Auguie and Barnes varied the amount of positional disorder in the nanoparticle array by 20%, 30%, and 40%. Pseudo-random configurations and full ordering were also observed. In each of these scenarios, the number of nanoparticles in the FOV was kept constant. The sparse arrays created in the present work looked at how the number of active nodes varied between different FOVs. Distribution of chain sizes is a direct reflection of the level of sparsity in the array. Multiple iterations of self-assembly could facilitate modulation of sparsity as well as possible

changes in nanoparticle concentration and lattice configuration.<sup>59</sup>

#### **4.5 One-Dimensional and Two-Dimensional Array Comparisons of Coupled Dipole Models with Experimental Results**

A comparison of experimental results from sparse arrays with computational simulations of homogenous arrays is important because it could bring forth understanding of effects due to perturbations from sparsity on CLR trends. Behaviors of sparse systems could lend value to areas of scientific literature where organization<sup>50</sup>, lattice parameter<sup>30,33,34,35</sup>, refractive index, and systems-level sensitivity<sup>12,89,90</sup> are studied for ordered metallic NPs.

An rsa-CDA model for homogenous 2D arrays consisting of varying numbers of AuNPs with a 38 nm radius, lattice spacing of 700 nm, and refractive index  $n = 1.45$  was performed. The results are compared with data obtained by Zou et al.<sup>35</sup> who used a CDA model and T-matrix model for homogenous 1D chains of varying numbers of silver NPs with a 50 nm radius. Both simulations show a logarithmic increase of CLR magnitudes with increasing number of NPs and can be seen in Figure 4.8. Only one particle per node was considered in both studies. T-matrix theory is a brute force, precise, but time consuming, numerical method that computes scattered fields for spherical particles whose size is on the order of the wavelength of light.<sup>91,92</sup> In comparison, rsa-CDA employs an analytical retarded dipole sum that decreases computational expense.

The number of NPs considered by Zou et al. was up to 450 silver particles whereas 2D arrays of up to 100,000 AuNPs were used for rsa-CDA (present work).<sup>89,31,32,93</sup> Experimental results are shown in the inset of Figure 4.8 and are contrasting to both computational results. The fabricated sparse systems exhibit a power law relation of CLR maxima versus number of optically active nodes. Diascopic (absorbance, 50x) and episcopic (counts, 100x) illumination

both exhibit this trend and could possibly result from cumulative backscattering effects from surrounding particles outside the FOV as well as the sparsity level of the system. Additional data points of greater than 1363 for episcopic illumination and 13223 for diascopic illumination could show a logarithmic trend because the data appears to possibly reach a logarithmic trend towards the higher end of the sparsity levels. However, limited equipment functionality prevents higher numbers of active nodes to be explored and future work aims at using both DDA and rsa-CDA to deepen the understanding of these sparse systems.<sup>59</sup>

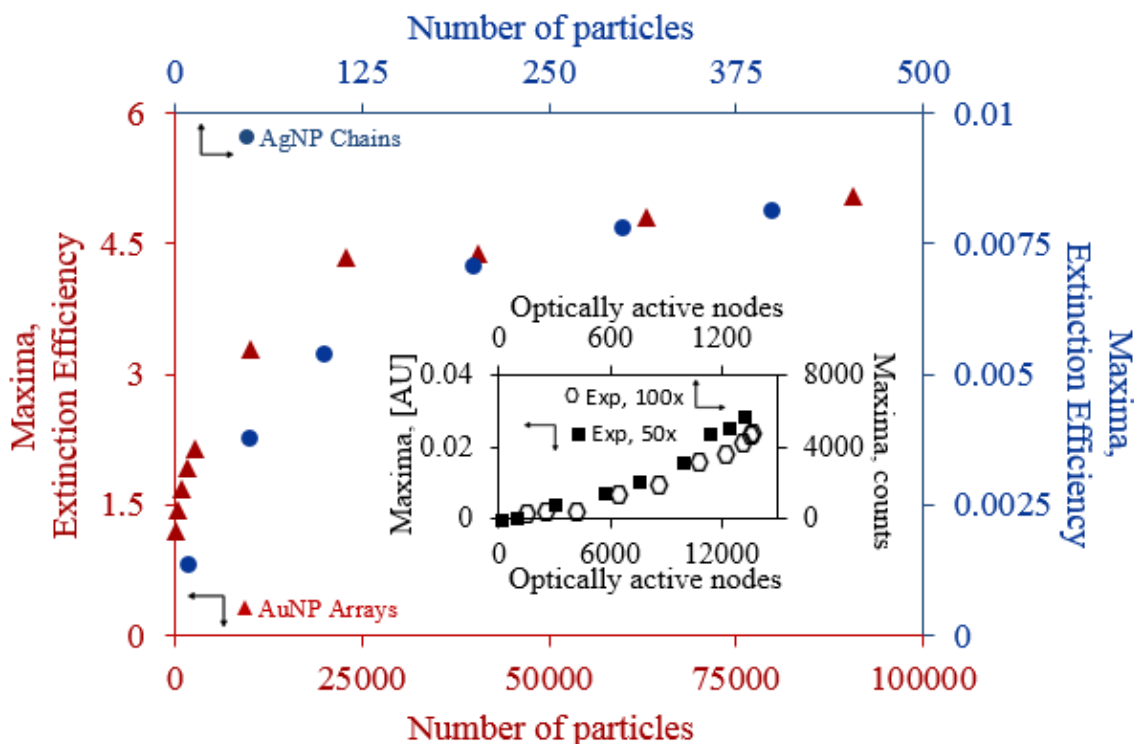


Figure 4.8. Logarithmic and non-linear intensity magnitude versus number of particles. Filled red triangles represents data obtained from rapid semi-analytical (rsa) coupled dipole approximation for gold nanoparticles in a two-dimensional array. Filled blue circles is data obtained from Zou et al.<sup>35</sup> for one-dimensional chains of silver nanoparticles. Inset shows the power law relation between CLR maximas for episcopic (hexagons) and diascopic (filled black squares) data obtained from the fabricated sparse arrays.<sup>59</sup>

#### 4.6 Summary

Diascopic and episcopic mode microscopy was performed to characterize the fabricated

sparse sample. A CLR was measured that red-shifted with increasing number of optically active nodes and the plasmon feature blue-shifted. As the number of optically active nodes increased in the field of view, and the sparsity decreased, the resonant coupling between the array plasmon and diffracted light got stronger and shifted the peak position of the resonance for the systems as described from the classical analogy. Manual counting and automated counting of optically active nodes helped to shed light on how the median chain size of optically active nodes can affect the resonances. Remarkably, despite sparsity existing in the array, the CLR was still measurable with as few as five optically active nodes in a chain on average. This agrees with the idea that emergent systems tend to be robust and resilient, especially when there are single point failures, such as those manifested from the sparsity in the array.

## **Chapter 5 - Concluding Remarks**

A novel, sparse array of gold nanoparticles exhibiting an emergent Fano resonant Couple Lattice Resonance was created and the research described in this thesis analyzed the effects of sparsity on the resonances of the system. Emergence was introduced and summarized briefly. A classical analogy previously described in literature for Fano resonance was utilized to help understand the behavior of the sparse system. Fabrication techniques were listed and described to differentiate why a self-assembly technique was used. Optical microscopy was performed to obtain images for analysis of how sparsity effected the resonances. A MATLAB subroutine was created to count particles in the captured images to correspond to spectra. Statistical analysis was performed on the results obtained from the MATLAB subroutine to identify median chain size and the minimum number of particles required for emergence of coupling to occur. This chapter will discuss the importance of the research performed, results obtained, and ideas for future work based on techniques used.

### **5.1 Importance of Work**

Understanding the effects of the number of nanoparticles on the emergence of Fano resonant Couple Lattice Resonance could help with the design of metamaterials that would be robust, and resilient to single point failures. The investigation of emergent behavior has been ongoing in the scientific community for decades. Schrodinger was among the first visionaries for the use of emergence in science to help understand how a system as a whole can operate distinctively different than the individual constituents. Emergence has even found a place in technology with NASA's ANTS mission that would send 1,000 robotic drones to explore the asteroid belt. One of the more particularly valuable areas is in biology. The TUNA program is

using the idea of emergence for applications such as using nanorobotic entities that would staunch a bleeding wound. This could have potential applications in the military, hospital emergencies, and even in home first aid emergencies. Emergent behavior appears to require a critical point for the behavior to be seen. Knowing the minimal value required to see emergent behavior in a system could possibly reduce fabrication cost, and increase device throughput. These ideas, however, have yet to be explored in literature and even though the research performed in this thesis discusses the idea based on nanoparticle arrays, more research is required.

## **5.2 Research Summary**

A novel, sparse array of gold nanoparticles was created and the effects of optically active node number on the array plasmon (AP) and coupled lattice resonance (CLR) were examined. As the number of optically active nodes increased in the field of view (FOV), the AP experienced a blue-shift in energy and the CLR red-shifted. The shifts in energy make sense when compared to the classical analogy of Fano resonance. When the broadband resonance (AP) and the discrete resonance (CLR) couple, there is an inherent shift in the natural frequency of the systems away from the isolated natural frequency. Single particle Mie theory for a 76 nm, gold nanoparticle with a polyvinylpyrrolidone capping suggests that the eigenmode energy in a PDMS-PEO medium is around 570 nm. For the created array, the eigenmode energy is approximately 550 nm which is an approximate 20 nm shift from theory. Equation 2.2 showed an approximation of this shift seen for a classical two particle system coupled weakly. Increasing the number of optically active nodes in the FOV caused a further shift as seen in Figures 4.2 and 4.4 for both diasopic and episopic microscopy. To understand this shift, one can examine the concepts derived in the

classical analogy. Increasing the number of optically active nodes increases the coupling parameter, as well as the damping coefficient, which pushes the eigenmode energy further red for the CLR and further blue for the AP. In short, more optically active nodes makes it easier for the system to scatter light in-plane because all optically active nodes are working together as a whole. As a result, there is an increased interference with the array plasmon causing the energy to blue-shift.

A list of different fabrication methods that are commonly used to create arrays of nanoparticles was discussed. Self-assembly of nanoparticles using soft-lithography techniques was employed for this research due to financial and equipment constraints. Soft-lithography uses a master stamp with the desired geometric configuration to pattern a polymer stamp. Polydimethylsiloxane (PDMS) is typically used for these types of experiments because it readily conforms to the pattern of the master stamp, does not degrade easily, is safe for use in biology applications, and is inexpensive. PDMS, however, has low surface free energy making it very hydrophobic. Techniques can be used to render PDMS surface hydrophilic such as sol-gel coatings and oxygen plasma but, due to PDMS's low glass transition temperature, these effects are short lived. This research used the block copolymer polydimethylsiloxane-block-polyethylene oxide (PDMS-b-PEO) to combine with base PDMS and make a hydrophilic stamp, a technique adapted from Yao et al. Water contact angles were decreased by five-fold making it easier for nanoparticle deposition by solution.

A silicon master stamp with a regular square array of cylindrical posts spaced 700 nm apart center-to-center was purchased for use in soft lithography of the sparse arrays. A hydrophilic solution of PDMS-PEO was created, added onto the master stamp, and allowed to cure. The resulting nanolithographed stamp had a regular lattice of cylindrical cavities spaced

700 nm apart center-to-center. Nanoparticle deposition was done by a simple continuous dewetting technique. The cured stamp had excess walls that surrounded the patterned area, making a well that the gold nanoparticle (AuNP) solution would be pipetted into. A glass microscope slide was used as the cover for the drying process; a 1/8<sup>th</sup> inch hole was drilled into the glass slide so the nanoparticle solution could be pipetted into the PDMS-PEO stamp. Drying took place for approximately two hours and particles were deposited due to a moving meniscus created by solution in contact with the glass cover, and patterned substrate. As the meniscus dried, particles were left deposited inside the cavities.

Images and spectra were captured in both episcopic and diasopic microscopy wherein each image a different number of optically active nodes was in the FOV. A MATLAB program was written to evaluate the luma of each image and use a threshold luma value to determine how many optically active nodes were in each image. The program also gave information on the size of each vertical chain of nodes. Because the light incident on the optically active nodes was horizontally polarized (x pol.), nodes in a vertical chain would couple with each other. Statistical analysis of chain size distributions showed that median chain sized increased with decreasing sparsity, as expected. Examination of chain size also showed an emergence of a Fano resonant coupled lattice resonance (CLR) with as few as five optically active nodes in a vertical chain. Extinction maxima versus number of optically active nodes increased by a power law relation. Theoretical discrete dipole approximate (DDA) for a two-dimensional array of particles with same size, in the same average dielectric constant, showed a logarithmic trend.

### **5.3 Future Work**

The sparse arrays fabricated in this research show promise for deepening the

understanding of emergent Fano resonant CLR of nanoparticle arrays. One particular area of interest for study with these samples is determining exactly how the coupling behaves between adjacent vertical chains of optically active nodes. For example, imagine having in one column a chain of 10 particles and a chain of 25 particles separated by only one empty node. Intuitively, one might posit that in the grand scheme of the system, missing one optically active node would not change the coupling between the two chains and it might not change the overall response very much, if at all. This would agree with what is currently known about emergent phenomena: emergent behavior is robust and is resilient to the failure of a single entity. On the other hand, there has to be a critical point by which the response of the system will begin to degrade. The results described in this thesis suggest that for the system created, PDMS-PEO array with 76 nm AuNPs capped with PVP, only a chain of 5 particles, on average, was required for the emergence of the coupling to occur. It could be that the responses gathered by the system were simply the addition of all the varying chain sizes. Further study is required to fully understand exactly how those missing nodal entities impact the response. A combination of DDA and rapid semi-analytic coupled dipole approximation (rsa-CDA) computational methods would be used to help with this understanding.

Another area of interest with these systems is in developing a mathematical framework to describe the system. This would prove to be a difficult task because every sparse array is different with random distributions of varying chain sizes. There is no particularly correct way to fabricate a sparse array. Because of this inherent difficulty, it might not be possible to develop a mathematical framework exactly, but perhaps numerical approximations could be used.

## References

1. Schneider, E. D. & Kay, J. J. *Order from Disorder: The Thermodynamics of Complexity in Biology. What is Life: The Next Fifty Years. Reflections on the Future of Biology.* 161-172. (Cambridge University Press, 1995). doi:10.1017/CBO9780511623295
2. Brogan, W. A. *Heidegger and Aristotle: The Twofoldness of Being.* 32. (State University of New York Press, 2005).
3. Schrödinger, E. *What is life? with Mind and Matter and Autobiographical Sketches.* 3-44. (Cambridge University Press, 1944). doi:10.2307/2019342
4. Huang, X. & El-Sayed, M. A. Plasmonic photo-thermal therapy (PPTT). *Alexandria J. Med.* **47**, 1–9 (2011).
5. Jørgensen, S. E. & Müller, F. *Handbook of Ecosystem Theories and Management.* 137-138. (Lewis Publishers, 2000).
6. Rouff, C., Vanderbilt, a., Truskowski, W., Rash, J. & Hinchey, M. Verification of NASA emergent systems. *Proceedings. Ninth IEEE Int. Conf. Eng. Complex Comput. Syst.* 1–8 (2004). doi:10.1109/ICECCS.2004.1310922
7. Stepney, S., Polack, F. A. C. & Turner, H. R. Engineering emergence. *11th IEEE Int. Conf. Eng. Complex Comput. Syst.* 9 (2006). doi:10.1109/ICECCS.2006.1690358
8. Lee, S.-H., Broholm, C., Ratcliff, W., Gasparovic, G., Huang, Q., Kim, T. H. & Cheong, S.-W. Emergent excitations in a geometrically frustrated magnet. *Nature* **418**, 856–858 (2002).
9. Hunter, A., Laursen, S. L. & Seymour, E. Becoming a scientist: The role of undergraduate research in students' cognitive, personal, and professional development. *Sci. Educ.* **91**, 36–74 (2007).
10. Ayyub, P. Aligned nanorod arrays: Additive and emergent properties. *J. Clust. Sci.* **20**, 429–451 (2009).
11. Brust, M. Nanoparticle ensembles: Nanocrystals come to order. *Nat. Mater.* **4**, 364–365 (2005).
12. Blake, P., Kühne, S., Forcherio, G. T. & Roper, D. K. Diffraction in nanoparticle lattices increases sensitivity of localized surface plasmon resonance to refractive index changes. *J. Nanophotonics* **8**, 83084 (2014).
13. Forcherio, G. T., Blake, P., DeJarnette, D. & Roper, D. K. Nanoring structure, spacing, and local dielectric sensitivity for plasmonic resonances in Fano resonant square lattices. *Opt. Express* **22**, 17791 (2014).

14. DeJarnette, D., Jang, G. G., Blake, P. & Roper, D. K. Polarization angle affects energy of plasmonic features in Fano resonant regular lattices. *J. Opt.* **16**, 105006 (2014).
15. Schuller, J. A., Barnard, E. S., Cai, W., Jun, Y. C., White, J. S. & Brongersma, M. L. Plasmonics for extreme light concentration and manipulation. *Nat. Mater.* **9**, 193–204 (2010).
16. Zhang, J. Z. & Noguez, C. Plasmonic optical properties and applications of metal nanostructures. *Plasmonics* **3**, 127–150 (2008).
17. Barnes, W. L., Dereux, A. & Ebbesen, T. W. Surface plasmon subwavelength optics. *Nature* **424**, 824–30 (2003).
18. Jain, P. K., Lee, K. S., El-Sayed, I. H. & El-Sayed, M. A. Calculated absorption and scattering properties of gold nanoparticles of different size, shape, and composition: Applications in biological imaging and biomedicine. *J. Phys. Chem. B* **110**, 7238–7248 (2006).
19. Link, S. & El-Sayed, M. A. Size and Temperature Dependence of the Plasmon Absorption of Colloidal Gold Nanoparticles. *J. Phys. Chem. B* **103**, 4212–4217 (1999).
20. Nehl, C. L. & Hafner, J. H. Shape-dependent plasmon resonances of gold nanoparticles. *J. Mater. Chem.* **18**, 2415 (2008).
21. Orendorff, C. J., Sau, T. K. & Murphy, C. J. Shape-dependent plasmon-resonant gold nanoparticles. *Small* **2**, 636–639 (2006).
22. Lombardi, J. R. & Birke, R. L. A unified approach to surface-enhanced raman spectroscopy. *J. Phys. Chem. C* **112**, 5605–5617 (2008).
23. Roper, D. K., Ahn, W. & Hoepfner, M. Microscale heat transfer transduced by surface plasmon resonant gold nanoparticles. *J. Phys. Chem. C* **111**, 3636–3641 (2007).
24. Baffou, G., Quidant, R. & García De Abajo, F. J. Nanoscale control of optical heating in complex plasmonic systems. *ACS Nano* **4**, 709–716 (2010).
25. Pissuwan, D., Valenzuela, S. M. & Cortie, M. B. Therapeutic possibilities of plasmonically heated gold nanoparticles. *Trends Biotechnol.* **24**, 62–67 (2006).
26. Atwater, H. A. & Polman, A. Plasmonics for improved photovoltaic devices. *Nat. Mater.* **9**, 865–865 (2010).
27. Anker, J. N., Hall, W. P., Lyandres, O., Shah, N. C., Zhao, J. & Van Duyne, R. P. Biosensing with plasmonic nanosensors. *Nat. Mater.* **7**, 442–453 (2008).
28. Roper, D. K., Ahn, W., Taylor, B. & Dall’Asen, A. G. Enhanced Spectral Sensing by Electromagnetic Coupling With Localized Surface Plasmons on Subwavelength Structures. *IEEE Sens. J.* **10**, 531–540 (2010).

29. Mayer, K. M. & Hafner, J. H. Localized surface plasmon resonance sensors. *Chem. Rev.* **111**, 3828–3857 (2011).
30. Auguie, B. & Barnes, W. L. Collective resonances in gold nanoparticle arrays. *Phys. Rev. Lett.* **101**, 143902 (2008).
31. DeJarnette, D., Roper, D. & Harbin, B. Geometric effects on far-field coupling between multipoles of nanoparticles in square arrays. *JOSA B* (2012).
32. DeJarnette, D., Norman, J. & Roper, D. K. Spectral patterns underlying polarization-enhanced diffractive interference are distinguishable by complex trigonometry. *Appl. Phys. Lett.* **101**, 183104 (2012).
33. Hicks, E. M., Zou, S., Schatz, G. C., Spears, K. G., Van Duyne, R. P., Gunnarsson, L., Rindzevicius, T., Kasemo, B. & Käll, M. Controlling plasmon line shapes through diffractive coupling in linear arrays of cylindrical nanoparticles fabricated by electron beam lithography. *Nano Lett.* **5**, 1065–1070 (2005).
34. Ross, M. B., Mirkin, C. A. & Schatz, G. C. Optical Properties of One-, Two-, and Three-Dimensional Arrays of Plasmonic Nanostructures. *J. Phys. Chem. C* **120**, acs.jpcc.5b10800 (2016).
35. Zou, S., Janel, N. & Schatz, G. C. Silver nanoparticle array structures that produce remarkably narrow plasmon lineshapes. *J. Chem. Phys.* **120**, 10871–10875 (2004).
36. Carron, K. T., Fluhr, W., Meier, M., Wokaun, a. & Lehmann, H. W. Resonances of two-dimensional particle gratings in surface-enhanced Raman scattering. *J. Opt. Soc. Am. B* **3**, 430 (1986).
37. Hohenau, A., Krenn, J. R., Beermann, J., Bozhevolnyi, S. I., Rodrigo, S. G., Martín-Moreno, L. & García-Vidal, F. Spectroscopy and nonlinear microscopy of Au nanoparticle arrays: Experiment and theory. *Phys. Rev. B - Condens. Matter Mater. Phys.* **73**, 155404 (2006).
38. Zhou, Y. & Zou, S. Effects of Dipole and Quadrupole Modes on the Switchable Total Transmission and Reflection in an Array of Rectangular Silver Prisms. *J. Phys. Chem. C* **120**, 20743–20748 (2016).
39. Artar, A., Yanik, A. A. & Altug, H. Directional double Fano resonances in plasmonic hetero-oligomers. *Nano Lett.* **11**, 3694–3700 (2011).
40. Francescato, Y., Giannini, V. & Maier, S. A. Plasmonic systems unveiled by fano resonances. *ACS Nano* **6**, 1830–1838 (2012).
41. Hao, F., Nordlander, P., Sonnefraud, Y., Van Dorpe, P. & Maier, S. A. Tunability of subradiant dipolar and fano-type plasmon resonances in metallic ring/disk cavities: Implications for nanoscale optical sensing. *ACS Nano* **3**, 643–652 (2009).

42. Verellen, N., Sonnefraud, Y., Sobhani, H., Hao, F., Moshehalkov, V. V., Van Dorpe, P., Nordlander, P. & Maier, S. A. Fano resonances in individual coherent plasmonic nanocavities. *Nano Lett.* **9**, 1663–1667 (2009).
43. Zheng, H., Vallee, R., Ly, I., Almeida, R. M., Rivera, T. & Ravaine, S. Morphological Design of Gold Nanopillar Arrays and Their Optical Properties. *J. Phys. Chem. C* **120**, 1178–1185 (2016).
44. Miroshnichenko, A. E. & Kivshar, Y. S. Engineering Fano resonances in discrete arrays. *Phys. Rev. E - Stat. Nonlinear, Soft Matter Phys.* **72**, 56611 (2005).
45. Albooyeh, M., Kruk, S. S., Menzel, C., Helgert, C., Kroll, M., Krysinski, A., Decker, M., Neshev, D. N., Pertsch, T., Etrich, C., Rockstuhl, C., Tretyakov, S. A., Simovski, C. R. & Kivshar, Y. S. Resonant metasurfaces at oblique incidence: interplay of order and disorder. *Sci. Rep.* **4**, 4484 (2014).
46. Helgert, C., Rockstuhl, C., Etrich, C., Kley, E. B., Tünnermann, A., Lederer, F. & Pertsch, T. Effects of anisotropic disorder in an optical metamaterial. *Appl. Phys. A Mater. Sci. Process.* **103**, 591–595 (2011).
47. Singh, R., Lu, X., Gu, J., Tian, Z. & Zhang, W. Random terahertz metamaterials. *J. Opt.* **12**, 15101 (2010).
48. Scheurer, M. S., Arnold, M. D., Setiadi, J. & Ford, M. J. Damping of plasmons of closely coupled sphere chains due to disordered gaps. *J. Phys. Chem. C* **116**, 1335–1343 (2012).
49. Antosiewicz, T. J. & Tarkowski, T. Localized Surface Plasmon Decay Pathways in Disordered Two-Dimensional Nanoparticle Arrays. *ACS Photonics* **2**, 1732–1738 (2015).
50. Auguié, B. & Barnes, W. L. Diffractive coupling in gold nanoparticle arrays and the effect of disorder. *Opt. Lett.* **34**, 401 (2009).
51. Fano, U. Effects of configuration interaction on intensities and phase shifts. *Phys. Rev.* **124**, 1866–1878 (1961).
52. Fano, U. On the absorption spectrum of noble gases at the arc spectrum limit. *arXiv Prepr. cond-mat/0502210* **161**, 154–161 (2005).
53. Joe, Y. S., Satanin, A. M. & Kim, C. S. Classical analogy of Fano resonances. *Phys. Scr.* **74**, 259 (2006).
54. Giannini, V., Francescato, Y., Amrania, H., Phillips, C. C. & Maier, S. A. Fano resonances in nanoscale plasmonic systems: A parameter-free modeling approach. *Nano Lett.* **11**, 2835–2840 (2011).
55. Mie, G. Beiträge zur Optik trüber Medien, speziell kolloidaler Metallösungen. *Ann. Phys.* **330**, 377–445 (1908).

56. Horvath, H. Gustav Mie and the scattering and absorption of light by particles: Historic developments and basics. *J. Quant. Spectrosc. Radiat. Transf.* **110**, 787–799 (2009).
57. Luk'yanchuk, B., Zheludev, N. I., Maier, S. a, Halas, N. J., Nordlander, P., Giessen, H. & Chong, C. T. The Fano resonance in plasmonic nanostructures and metamaterials. *Nat. Mater.* **9**, 707–15 (2010).
58. French, R. T., Bejugam, V., Forcherio, G. T. & Roper, D. K. Supporting Information 'Optical characteristics of a lattice resonance supported by plasmonic nanoparticles deposited sparsely in a nanoimprinted polymer'. *J. Quant. Spectrosc. Radiat. Transf.* Submitted, Under Review. (2017).
59. French, R. T., Bejugam, V., Forcherio, G. T. & Roper, D. K. Optical characteristics of a lattice resonance supported by plasmonic nanoparticles deposited sparsely in a nanoimprinted polymer. *J. Quant. Spectrosc. Radiat. Transf.* Submitted, Under Review. (2017).
60. Altissimo, M. E-beam lithography for micro-/nanofabrication. *Biomicrofluidics* **4**, 26503 (2010).
61. Schiff, H. Nanoimprint lithography: An old story in modern times? A review. *J. Vac. Sci. Technol. B Microelectron. Nanom. Struct.* **26**, 458 (2008).
62. Colson, P., Henrist, C. & Cloots, R. Nanosphere Lithography : A Powerful Method for the Controlled Manufacturing of Nanomaterials. *J. Nanomater.* **2013**, 1-19 (2013).
63. Nagpal, P., Lindquist, N. C., Oh, S.-H. & Norris, D. J. Ultrasoother patterned metals for plasmonics and metamaterials. *Science* **325**, 594–7 (2009).
64. Fan, J. A., Bao, K., Sun, L., Bao, J., Manoharan, V. N., Nordlander, P. & Capasso, F. Plasmonic mode engineering with templated self-assembled nanoclusters. *Nano Lett.* **12**, 5318–5324 (2012).
65. Malaquin, L., Kraus, T., Schmid, H., Delamarche, E. & Wolf, H. Controlled particle placement through convective and capillary assembly. *Langmuir* **23**, 11513–11521 (2007).
66. Yin, Y., Lu, Y., Gates, B. & Xia, Y. Template-assisted self-assembly: A practical route to complex aggregates of monodispersed colloids with well-defined sizes, shapes, and structures. *J. Am. Chem. Soc.* **123**, 8718–8729 (2001).
67. Juillerat, F., Solak, H. H., Bowen, P. & Hofmann, H. Fabrication of large-area ordered arrays of nanoparticles on patterned substrates. *Nanotechnology* **16**, 1311–1316 (2005).
68. Cui, Y., Björk, M. T., Liddle, J. A., Sönnichsen, C., Boussert, B. & Alivisatos, A. P. Integration of colloidal nanocrystals into lithographically patterned devices. *Nano Lett.* **4**, 1093–1098 (2004).
69. Kraus, T., Malaquin, L., Schmid, H., Riess, W., Spencer, N. D. & Wolf, H. Nanoparticle

- printing with single-particle resolution. *Nat. Nanotechnol.* **2**, 570–6 (2007).
70. Mahalingam, V., Onclin, S., Péter, M., Ravoo, B. J., Huskens, J. & Reinhoudt, D. N. Directed self-assembly of functionalized silica nanoparticles on molecular printboards through multivalent supramolecular interactions. *Langmuir* **20**, 11756–11762 (2004).
  71. Prevo, B. G., Hwang, Y. & Velev, O. D. Convective assembly of antireflective silica coatings with controlled thickness and refractive index. *Chem. Mater.* **17**, 3642–3651 (2005).
  72. Denkov, N., Velev, O., Kralchevski, P., Ivanov, I., Yoshimura, H. & Nagayama, K. Mechanism of formation of two-dimensional crystals from latex particles on substrates. *Langmuir* **8**, 3183–3190 (1992).
  73. Hillborg, H. & Gedde, U. Hydrophobicity Changes in Silicone Rubbers. *IEEE Trans. Dielectr.* **6**, 703–717 (1999).
  74. Vargaftik, N. B., Volkov, B. N. & Voljak, L. D. International Tables of the Surface Tension of Water. *J. Phys. Chem. Ref. Data* **12**, 817–820 (1983).
  75. Zhou, J., Ellis, A. V. & Voelcker, N. H. Recent developments in PDMS surface modification for microfluidic devices. *Electrophoresis* **31**, 2–16 (2010).
  76. Wong, I. & Ho, C. M. Surface molecular property modifications for poly(dimethylsiloxane) (PDMS) based microfluidic devices. *Microfluid. Nanofluidics* **7**, 291–306 (2009).
  77. Yao, M. & Fang, J. Hydrophilic PEO-PDMS for microfluidic applications. *J. Micromechanics Microengineering* **22**, 25012 (2012).
  78. Yu, K. & Han, Y. A stable PEO-tethered PDMS surface having controllable wetting property by a swelling-deswelling process. *Soft Matter* **2**, 705 (2006).
  79. Pedersen, J., Steinkuhler, C., Wesser, U. & Rotilio, G. Rasband, WS, ImageJ, US National Institutes of Health, Bethesda, Maryland, USA. *imagej.nih.gov/ij* (2011).
  80. Schneider, C. a, Rasband, W. S. & Eliceiri, K. W. NIH Image to ImageJ: 25 years of image analysis. *Nat. Methods* **9**, 671–675 (2012).
  81. Breckon, C. S. T. *Fundamentals of Digital Image Processing : a Practical Approach with Examples in Matlab*. 344. (John Wiley & Sons Inc., 2011).
  82. Carpenter, A. E., Jones, T. R., Lamprecht, M. R., Clarke, C., Kang, I. H., Friman, O., Guertin, D. a, Chang, J. H., Lindquist, R. a, Moffat, J., Golland, P. & Sabatini, D. M. CellProfiler: image analysis software for identifying and quantifying cell phenotypes. *Genome Biol.* **7**, R100 (2006).
  83. Poynton, C. *Digital Video and HDTV: Algorithms and Interfaces*. 752. (Elsevier, 2003).

84. Jacobson, R. *Color Image Processing and Applications. Measurement Science and Technology* **12**, (Springer Berlin Heidelberg, 2001).
85. Chen, G. H., Chen, W. Y., Yen, Y. C., Wang, C. W., Chang, H. T. & Chen, C. F. Detection of mercury(II) ions using colorimetric gold nanoparticles on paper-based analytical devices. *Anal. Chem.* **86**, 6843–6849 (2014).
86. Cheng, X., Dai, D., Yuan, Z., Peng, L., He, Y. & Yeung, E. S. Color difference amplification between gold nanoparticles in colorimetric analysis with actively controlled multiband illumination. *Anal. Chem.* **86**, 7584–7592 (2014).
87. King, N. S., Liu, L., Yang, X., Cerjan, B., Everitt, H. O., Nordlander, P. & Halas, N. J. Fano Resonant Aluminum Nanoclusters for Plasmonic Colorimetric Sensing. *ACS Nano* **9**, 10628–10636 (2015).
88. Kovács, R. American Association for the Advancement of Science. *JSTOR* **54**, 155–161 (2014).
89. Blake, P., Obermann, J., Harbin, B. & Roper, D. K. Enhanced nanoparticle response from coupled dipole excitation for plasmon sensors. *IEEE Sens. J.* **11**, 3332–3340 (2011).
90. Auguié, B., Bendaña, X. M., Barnes, W. L. & García de Abajo, F. J. Diffractive arrays of gold nanoparticles near an interface: Critical role of the substrate. *Phys. Rev. B* **82**, 155447 (2010).
91. Parsons, J., Burrows, C. P., Sambles, J. R. & Barnes, W. L. A comparison of techniques used to simulate the scattering of electromagnetic radiation by metallic nanostructures. *J. Mod. Opt.* **57**, 356–365 (2010).
92. Somerville, W. R. C., Auguié, B. & Le Ru, E. C. Simplified expressions of the T-matrix integrals for electromagnetic scattering. *Opt. Lett.* **36**, 3482–4 (2011).
93. DeJarnette, D., Norman, J. & Roper, D. K. Attribution of Fano resonant features to plasmonic particle size, lattice constant, and dielectric wavenumber in square nanoparticle lattices. *Photonics Res.* **2**, 15 (2014).

## APPENDIX

### A: Description of Research for Popular Publication

Since the advent of the first transistor, technology has inevitably moved toward smaller and smaller scales of fabrication. This idea is seen every year when mobile phone companies present keynote presentations discussing how slim the next model of mobile phone is going to be and all of the new, cool features it will have, such as a better camera.

The shrinking of technology has caused scientists for the past several decades to explore the area of Nanotechnology. Progress made in this area has shown promise in new and powerful designs of solar cells, biological sensors, chemical sensors, etc. Roy T. French III, a student in the Microelectronics-Photonics Master's program is studying the emergence of spectral features of a sparse array of nanoparticles from excitation due to light.

Because the particles are arranged in an array, two features can be measured: one from the oscillation of electrons in the metal nanoparticles, and a second from the scattering of light due to the array. These two features could be useful for sensing of biologicals, and chemicals because they allow for a much broader range of light that can be absorbed, and/or scattered.

With the help from his advisor Dr. D. Keith Roper, and his colleagues Vinith Bejugam, and Gregory Forcherio, samples have been fabricated of sparse arrays containing gold metal nanoparticles in a biocompatible polymer that exhibit both types of spectral features previously mentioned.

This was achieved by taking a prepatterned master stamp with cylindrical posts spaced 700 nm apart and using a hydrophilic polymer solution to create a polymer stamp. The resulting stamp creates an inverted pattern from the master stamp. This means that the polymer stamp, when dried, would have cylindrical cavities spaced 700 nm apart instead of posts.

An aqueous solution of gold nanoparticles was added to the polymer stamp for template-based self-assembly where the particles assembled into the cavities, creating a sparse array.

Characterization of the samples showed that having a minimum of five particles consecutively in a chain can give rise to both responses mentioned above. This notion has not yet been studied, and could give insight for engineers when making systems like these as sensors. Knowing the minimum number required to give a good response could cut down on materials, cost, and waste.

## **B: Executive Summary of Newly Created Intellectual Property**

Below is a list of newly created intellectual items.

1. Fabrication of a sparse array of gold nanoparticles in a polydimethylsiloxane-polyethylene oxide polymer medium.
2. Creation of a MATLAB program to help with counting nanoparticles in an image.

## **C: Possible Patent and Commercialization Aspects of Intellectual Property**

### ***C.1 Patentability of Intellectual Property***

Each of the following items were considered for potential patentability. It was determined that none of the above items could be patented. Detail descriptions follow.

1. The sparse array of gold nanoparticles in a PDMS-PEO medium was created using commercially available materials. However, the deposition techniques used for deposition were obtained from literature. There were no new ideas for the deposition of the particles to obtain unique sparse arrays. The sparsity was obtained by random deposition and therefore the array has been determined to not be patentable.
2. The MATLAB program created to count particles is a unique contribution to the scientific community. However, the program utilizes equipment calibrations from a microscope camera. Not all cameras would have the same calibrations and as such it would be best to not patent the program as it is not general enough to apply to a broader range of equipment.

### ***C.2 Commercialization Aspects***

Each item of Appendix B was considered for commercialization opportunities. It was determined that none of them have commercial appeal. Detail descriptions follow.

1. The sparse array of gold nanoparticles does have commercialization viability. However, it would require fine-tuning to properly deposit a specific type of sparse array. As it stands, the sparse array is too random and there is not a true reproducibility. This would need to be properly studied to find a way to create a reproducible sparse array.
2. The MATLAB program created to count particles does have commercialization viability. However, other research organizations could create similar programs for their purposes.

As such the program would be best suited as a template for counting particles of microscope images and allowed to be public access.

### ***C.3 Possible Future Disclosure of Intellectual Property***

Both the sparse array created in a PDMS-PEO medium and the MATLAB program is currently being prepared for publication in the Journal of Quantitative Spectroscopy and Radiative Transfer. First authorship will belong to Roy T. French III and Vinith Bejugam. Gregory T. Forcherio is co-author.

## **D: Broader Impact of Research**

### ***D.1 Applicability of Research Methods to Other Problems***

All of the ideas and concepts discussed in thesis could be applied to areas such as biological sensors, chemical sensors, solar cells, and other optoelectronic devices. For example, there is currently a desire for using arrays of gold nanoparticles exhibiting emergent Fano resonant Coupled Lattice Resonance as biological sensors. Because sparse arrays act as scattering potentials where nodal elements are missing, it could be possible that a larger resonant response could be measured for those biological sensors.

### ***D.2 Impact of Research Results on U.S. and Global Society***

Currently, emergent behavior is being studied by NASA for designing robotic devices that would work together to study the asteroid belt.<sup>1</sup> The Computer Science Department at University of York has created the Theory Underpinning Nanotech Assembly project.<sup>2</sup> This project aims to help develop engineering tools and a process for creating emergent systems by using case studies. One of the case studies is in regards to clotting wounds using nanorobots. This has potential applications in medicine and military. This work could help with concepts and development processes to engineer emergent systems for use in optoelectronic devices, biological sensors, and chemical sensors.

### ***D.3. Impact of Research Results on the Environment***

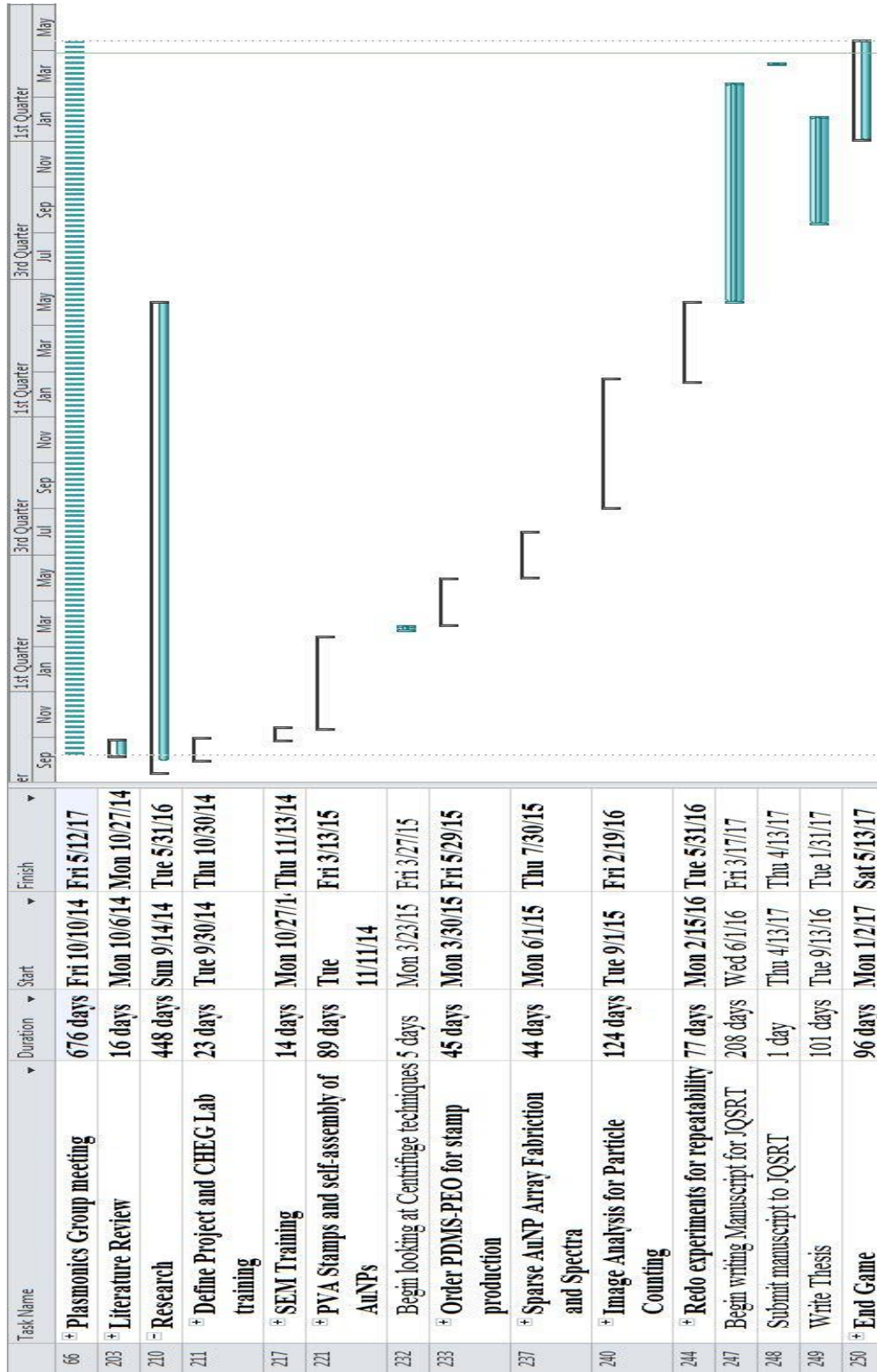
Reduction of carbon waste generated by burning fossil fuels for energy is one of the biggest problems scientists are currently facing and will face in the future. Great strides have been made to create more efficient solar cells that would harness renewable solar radiation to

convert it to electricity. The sparse arrays generated in this research could have applications in this field because of the two distinguishable resonant responses that can be measured. The arrays possibly could help with scattering light in-plane to the array allowing for greater capture of light. The resonant profiles are spectrally broad as well, so a larger range of wavelengths could be captured. Using solar cells helps reduce carbon emissions.

#### REFERENCES

1. Rouff, C., Vanderbilt, a., Truskowski, W., Rash, J. & Hinchey, M. Verification of NASA emergent systems. *Proceedings. Ninth IEEE Int. Conf. Eng. Complex Comput. Syst.* 1–8 (2004). doi:10.1109/ICECCS.2004.1310922
2. Stepney, S., Polack, F. A. C. & Turner, H. R. Engineering emergence. *11th IEEE Int. Conf. Eng. Complex Comput. Syst.* 9 (2006). doi:10.1109/ICECCS.2006.1690358

## E: Microsoft Project for Master's Microelectronics-Photonics Degree Plan



## **F: Identification of All Software Used in Thesis Generation**

### Computer #1:

Model: Dell E173FPs  
Serial Number: CN-0F7170-47606-4CM-ATL4  
University of Arkansas Number: 7045027  
Location: Bell Engineering, Room 2211  
Owner: Department of Chemical Engineering, University of Arkansas

### Software #1:

Name: Matlab R2016b  
Purchased By: Department of Chemical Engineering, University of Arkansas  
License Number: 601103

### Computer #2:

Model: Dell Inspiron 15 Laptop  
Serial Number: 5L2B1C2  
Location: Home  
Owner: Roy T. French III

### Software #1:

Name: Microsoft Office 2016  
Purchased By: Roy T. French III

### Software #2:

Name: Mendeley (v1.17.8)  
Purchased By: Roy T. French III  
License: Freeware

### Software #3:

Name: ImageJ  
Purchased By: Roy T. French III  
License: Freeware

## **G: All Publications Published, Submitted, and Planned**

### Publication Submitted

- Roy T. French III, Vinith Bejugam, Gregory T. Forcherio, and D.K. Roper, “Optical Characteristics of a Lattice Resonance Supported by Plasmonic Nanoparticles Deposited Sparsely in a Nanoimprinted Polymer.” Submitted to Journal of Quantitative Spectroscopy and Radiative Transfer.